JOURNAL OF GEOPHYSICAL RESEARCH SPACE PHYSICS, VOL. 121, 2016, DOI:10.1002/2015JA021764

Nucleation of mesospheric cloud particles: Sensitivities and limits

Henrike Wilms,[1] Markus Rapp,[1,2] Annekatrin Kirsch[3]

- Influence of nucleation rate on NLC properties is studied with CARMA
- Realistic NLC can be modelled if nucleation rate is reduced by several orders of magnitude
- Background wind limits the lifetime of ice particles

Corresponding author: Henrike Wilms, German Aerospace Center, Institute of Atmospheric Physics, Münchner Straße 20, 82234 Weßling, Germany. (Henrike.Wilms@dlr.de)

[1]Deutsches Zentrum für Luft- und Raumfahrt, Institut für Physik der Atmosphäre, Oberpfaffenhofen, Germany

[2]Also at Meteorologisches Institut München, Ludwig-Maximilians-Universität München, Munich, Germany

[3]Leibniz-Institute of Atmospheric Physics at Rostock University, Kühlungsborn, Germany

Abstract.

Nucleation of mesospheric ice particles is thought to occur via heterogeneous nucleation on meteor smoke particles. However, several factors determining the nucleation rate are poorly known. To study the effect of uncertainties in the nucleation rate on cloud properties, we use the Community Aerosol and Radiation Model for Atmospheres and systematically vary the nucleation rate over ±10 orders of magnitude. In one set of simulations, the background state of the atmosphere is described by climatological conditions. In a second set, gravity wave perturbed profiles from the Kühlungsborn Mechanistic general Circulation Model (KMCM) are used with typical temperature (vertical wind) perturbations at the mesopause on the order of 9 K (0.45 m/s). The resulting noctilucent cloud (NLC) characteristics are compared to lidar and satellite measurements. Realistic NLC compared to the lidar measurements can only be modelled if the nucleation rate is reduced by up to 3 orders of magnitude compared to standard assumptions. For the same cases, the simulated NLC compare best to the satellite measurements if the nucleation rate is reduced by 2 orders of magnitude or more.

Dynamical processes at the mesopause strongly influence the NLC development. In a gravity wave perturbed atmosphere, the ice particles have only limited time for nucleation and growth. The growth time is limited by the vertical wind, because the vertical wind determines the residence time of the ice particles in the supersaturated region. Since the vertical wind amplitudes reach 1.5 m/s in KMCM (compared to a mean upwelling of $\sim$ 4 cm/s in

the climatology), the ice particles remain significantly smaller in a gravity wave perturbed atmosphere than in climatological background conditions.

1. Introduction

The extreme conditions of the cold polar summer mesopause enable the formation of mesospheric ice particles. Observed from the ground they are called noctilucent clouds (NLC) or when observed from space they are named polar mesospheric clouds (PMC). For simplicity, we refer to mesospheric clouds as NLC throughout this paper. NLC observations offer the unique possibility to study processes of the mesopause region, which are difficult to access otherwise. In particular, dynamical properties are commonly inferred from NLC measurements. For example, wave parameters and wind velocities have been determined from ground based NLC photography [e.g., *Witt*, 1962; *Pautet et al.*, 2011], from NLC lidar measurements [e.g., *Kaifler et al.*, 2013a], and from satellite measurements of NLC [e.g., *Chandran et al.*, 2009; *Rong et al.*, 2015]. Kelvin-Helmholtz instabilities have been identified to cause small scale structures of NLC [*Baumgarten and Fritts*, 2014]. The underlying assumption for all these studies is that NLC can be treated as a passive tracer. *Baumgarten et al.* [2012] reported coincident lidar and satellite measurements and found that NLC can be treated as a passive tracer for time scales of about 1 h and less. In the study of *Chandran et al.* [2012] significant changes of NLC albedo were analysed, which occurred on time scales of 1.5 h between subsequent satellite overpasses. These changes in NLC albedo are possibly related to ice particles growing from subvisible to visible sizes [*Chandran et al.*, 2012], indicating that NLC cannot be considered as a passive tracer for these longer time scales.

In order to precisely determine to what extent and on which temporal scales NLC can be considered as a passive tracer, the microphysical processes including their dependence on

dynamical perturbations (and corresponding thermal perturbations) must be thoroughly understood.

The microphysical process which is least quantified is the initial ice formation, i.e. the nucleation of mesospheric ice particles [*Thomas*, 1991; *Rapp and Thomas*, 2006]. Several different nucleation pathways for mesospheric ice particles have been proposed in the past. Among them are heterogeneous nucleation [e.g., *Turco et al.*, 1982], homogeneous nucleation [e.g., *Murray and Jensen*, 2010], nucleation on ionic water clusters [*Witt*, 1969], as well as nucleation on strongly bipolar molecules such as $NaHCO_3$ [*Plane*, 2000].

In the case of heterogeneous nucleation ice particles form on preexisting ice nuclei. Ice nuclei lower the energy barrier associated with the phase change [*Pruppacher and Klett*, 1997]. The most likely candidate for meospheric ice nuclei are meteor smoke particles (MSP), which are thought to form from the material of ablated meteoroids [*Hunten et al.*, 1980]. The picture of the ubiquitous and numerous abundance of sufficiently large MSP in the polar mesosphere has been challenged by *Megner et al.* [2008a], who found that during summer MSP are effectively transported to lower latitudes before coagulating to sizes relevant for nucleation.

The energy barrier can also be reduced or even be removed due to Coulomb interactions if the nucleation process involves ions (e.g., proton hydrates $H^+(H_2O)_n$) or charged MSP. Ionic nucleation is limited by the recombination with free electrons [*Sugiyama*, 1994]. However, *Gumbel and Witt* [2002] found a positive feedback mechanism for ionic nucleation, when ice particles are already present: The initial ice particles capture free electrons, which reduces the recombination of proton hydrate clusters with electrons. Under these

conditions ion induced nucleation can become efficient, amplifying initial variations in ice particle, ion or electron density.

Nucleation on charged MSP could solve the problem of potentially sparse MSP number densities [*Megner et al.*, 2008a]. This is because the MSP charge results in a reduction of the energy barrier for nucleation and may even result in a complete vanishing of this barrier depending on ambient conditions of supersaturation. Thus even smaller MSP can act as ice nuclei when they are charged compared to when they are uncharged. The nucleation on charged MSP has been discussed in detail by *Gumbel and Megner* [2009] and *Megner and Gumbel* [2009].

Nucleation can also occur without the presence of preexisting ice nuclei or ions, which is then called homogeneous nucleation. Homogeneous nucleation generally requires more extreme conditions compared to heterogeneous nucleation, i.e., lower temperatures and higher saturation ratios. Heterogeneous nucleation therefore is more likely if ice nuclei are present. Heterogeneously nucleated ice particles will consume part of the available water vapor before homogeneous nucleation sets in. The main factor which determines how much water vapor will already be consumed is the cooling rate, e.g., cooling induced by waves. *Murray and Jensen* [2010] showed that homogeneous nucleation can compete with heterogeneous nucleation for cooling rates larger than 0.5 K/h at ambient temperatures below 110 K. In these cases, the onset of homogeneous nucleation occurs before heterogeneous nucleation has depleted the available water vapor.

From these possible nucleation pathways heterogeneous nucleation on MSP is considered to be the most likely one [*Rapp and Thomas*, 2006]. *Hervig et al.* [2012] infer from observations that mesospheric ice particles contain small amounts of meteoric smoke,

which confirms the assumption that MSP are involved in the microphysical processes. Still, it is yet to be demonstrated whether the MSP act as nucleation sites or are collected by the growing ice particles after nucleation.

On top of our lack of knowledge of the exact nucleation pathway, the parameters that determine the nucleation rate itself are poorly known, because laboratory measurements under mesospheric conditions are rare. Nevertheless, *Merkel et al.* [2009] have successfully modelled the global distribution of PMC and their optical properties without explicitly calculating nucleation and growth rates. *Megner* [2011] concluded that observable NLC properties are basically independent of the nucleation conditions. These studies pose the question whether in the end the details of the nucleation process are truly important for the development of NLC.

In this study we analyse to what extent the nucleation process determines the properties of the resulting NLC. This study builds on the comprehensive sensitivity study by *Rapp and Thomas* [2006] with an explicit focus on the sensitivity of NLC properties on the nucleation rate. We model NLC with the Community Aerosol and Radiation Model for Atmospheres (CARMA) using a wide range of nucleation rates. The modelled NLC are then compared to lidar measurements from the Arctic Lidar Observatory for Middle Atmosphere Research (ALOMAR) and to satellite measurements by the Solar Occultation For Ice Experiment (SOFIE) onboard the Aeronomy of Ice in the Mesosphere (AIM) satellite and to measurements by the Optical Spectrograph and InfraRed Imager System (OSIRIS) onboard the Odin satellite. This comparison modelled NLC with lidar and satellite observations allows us to constrain the nucleation rate through other unknown quantities, such as the availability of MSP. The microphysical model CARMA has been

updated from the version used by *Rapp and Thomas* [2006] by including a more advanced MSP profile and by implementing wave driven background fields. The MSP profile is now taken from the global MSP model by *Megner et al.* [2008b], which has significantly lower number densities than the previously used profile by *Hunten et al.* [1980] (i.e., the number density of MSP larger than 1 nm is now 1% of the *Hunten et al.* [1980] profile or less). The wave driven background fields are taken from the Kühlungsborn Mechanistic general Circulation Model (KMCM) with RMS (root mean square) values of temperature and vertical wind fluctuations at the mesopause of 9 K and 0.45 m/s, respectively. The strong variability of temperature and vertical wind constrains nucleation and growth times. This setup is significantly different from simulations with climatological background profiles where the ice particles have in principal unlimited time to deplete the available water vapor, since their lifetime is only limited by sedimentation. With wave driven background fields the parameters that determine the microphysical time constants gain importance. One of these is the nucleation rate which is the major subject of this study.

First, we discuss the currently assumed expression for the nucleation rate and all unknown parameters in Section 2. This motivates the range of nucleation rates we subsequently implement in CARMA. The CARMA model and the setup of our sensitivity experiments are described in Section 3. Basic dependencies derived from simulations in climatological and wave driven conditions as well as the comparison of modelled NLC with observations are presented in Section 4. In Section 5 we discuss our results in the context of other studies and summarize the main results in Section 6.

2. Nucleation Theory

Meteoric smoke particles (MSP) are the most likely candidate for ice nuclei in the mesopause region (see *Rapp and Thomas* [2006] for a discussion of other candidates). According to classical nucleation theory water molecules are adsorbed onto the surface of MSP and form clusters which grow by the attachment of additional molecules. As soon as a cluster exceeds the critical radius r^*, further growth is on average energetically favored in a supersaturated environment and the ice particle continues growing. The nucleation rate J can be expressed as [*Keesee*, 1989]

$$J = \frac{Z\bar{\delta}r^* \sin\theta}{\nu m_\mathrm{w} kT} p_{\mathrm{H_2O}}^2 4\pi r_\mathrm{N}^2 [N_\mathrm{N}] \cdot \exp\left(\frac{2\Delta F_\mathrm{des} - \Delta F_\mathrm{sd} - f\Delta F^*}{kT}\right) \quad (1)$$

with the critical radius r^* and associated energy barrier ΔF^* needed to form a cluster of radius r^*

$$r^* = \frac{2m_\mathrm{w}\sigma}{kT\rho_\mathrm{ice}\ln S} \quad (2)$$

$$\Delta F^* = \frac{4}{3}\pi\sigma r^{*2} = \frac{16\pi\sigma^3 m_\mathrm{w}^2}{3(kT\rho_\mathrm{ice}\ln S)^2}. \quad (3)$$

Atmospheric conditions such as the temperature T, the water vapor partial pressure $p_{\mathrm{H_2O}}$ and the saturation ratio S directly enter the nucleation rate, as well as properties of the nucleus like the contact angle θ, the desorption energy ΔF_des, the activation energy for surface diffusion ΔF_sd, the mean diffusional jump distance of an adsorbed water molecule $\bar{\delta}$, the vibration frequency of an adsorbed water molecule ν, the radius of the nucleus r_N, and the number density of nuclei $[N_\mathrm{N}]$. The Fletcher factor f [*Fletcher*, 1958, 1959] accounts for the fact that only an ice cap needs to be formed instead of a complete sphere which is implicitly assumed by the derivation of ΔF^*. f is a function of the contact parameter $m = \cos\theta$ and the ratio r_N/r^*. The Zeldovich factor Z [*Zeldovich*, 1942; *Pruppacher and Klett*, 1997] corrects non equilibrium effects in the size distribution

of clusters on the nuclei surface and determines the percentage of critical clusters that become stable clusters. *Vehkamäki et al.* [2007] give an exact formulation of the Zeldovich factor for heterogeneous nucleation on a spherical nucleus. The properties of the condensed phase are considered via the surface energy σ, the mass of one water molecule m_{w} and the ice density ρ_{ice}. Finally, k denotes the Boltzmann constant.

The nucleation rate as expressed above relies on several assumptions, where the application to mesospheric conditions is questionable. First of all, the capillarity approximation – the fundamental assumption of classical nucleation theory – treats a cluster as a macroscopic object with the characteristics of the bulk material. The physical concept of surface tension, which proves to be useful for the description of macroscopic objects, is applied to systems in the size of nanometers. The ice cap of a critical cluster with $r^* = 1.1$ nm on a 1.2 nm nucleus with $m = 0.95$ contains only $n^* = V^* \rho_{\mathrm{ice}}/m_{\mathrm{w}} \approx 30$ molecules. In this size regime of only a few molecules, the explicit interaction of molecules is likely to become important as well as the contribution of rotational and translational energy to the total free energy of the cluster [e.g., *Lee et al.*, 1973]. Additionally, the surface tension for a planar surface is used in classical nucleation theory, which is not corrected for curvature effects as introduced by *Tolman* [1949]. Even if the capillarity approximation proves to be correct, the surface tension has not been measured in the relevant temperature range. The parametrization by *Hale and Plummer* [1974] is commonly used for microphysical calculations of NLC [*Turco et al.*, 1982; *Berger and Zahn*, 2002]. However, the parametrization is based on a linear extrapolation from measurements performed above 235 K.

When applying classical nucleation theory to heterogeneous nucleation on MSP, ice nuclei are assumed to be perfect spheres with no surface inhomogeneities. This implies

that there are no preferred nucleation sites and no barriers for surface diffusion. However, laboratory experiments of meteor smoke analogues by *Saunders and Plane* [2006] revealed that iron containing MSP (which are currently deemed to be likely candidates for MSP composition, *Hervig et al.* [2012]) have an amorphous structure and are fractal and chain like. This is completely contrary to the theoretical assumptions.

The contact angle, which enters the nucleation rate via m, describes how 'wettable' a surface is or how well the lattices of nucleus and ice fit to each other. *Roddy* [1984] systematically searched for substances that have crystal structures similar to cubic ice and thus have a small misfit parameter. For wüstite (FeO) and other meteoric materials the misfit parameter is comparable to the misfit parameter of silver iodide, which is a very efficient ice nucleus for hexagonal ice [*Vonnegut*, 1947]. Therefore MSP are assumed to be efficient ice nuclei as well and a large value of $m = 0.95$ [e.g., *Rapp and Thomas*, 2006; *Bardeen et al.*, 2010] or $m = 0.97$ [*Määttänen et al.*, 2005; *Wood*, 1999] has been chosen in previous modelling studies of mesospheric ice clouds. However, *Bardeen et al.* [2010] have also varied m over a wide range to reflect the large uncertainty of the contact parameter. *Trainer et al.* [2009] deduced the temperature dependence of m based on laboratory measurements on a monocrystalline silicon wafer and the applicability of classical nucleation theory. They find contact parameters as low as 0.6 for temperatures of 150 K. In the mesopause region with temperatures around 130 K even smaller values for m would be expected, based on the temperature trend found by *Trainer et al.* [2009]. Changing m from 0.95 to only 0.93 reduces the nucleation rate by three orders of magnitude. This demonstrates the high sensitivity of the nucleation rate on m and consequently also the uncertainty introduced by the contact angle.

Classical nucleation theory further assumes that the temperature of the substrate is equal to the temperature of the surrounding gas. However, MSP can be significantly warmer than the ambient atmosphere [*Fiocco et al.*, 1975; *Eidhammer and Havnes*, 2001; *Asmus et al.*, 2014]. Depending on composition and especially iron content, a 1.2 nm MSP can reach a temperature offset of up to 10 K. A temperature offset of only 1 K leads to a reduction of the nucleation rate by five orders of magnitude [*Asmus et al.*, 2014].

Another critical parameter, if not the most critical parameter, is the desorption energy ΔF_{des} as it occurs in the exponential term of Eq. 1 with a positive sign. The value of $\Delta F_{\mathrm{des}} = 2.9 \cdot 10^{-20}$ J which is commonly used [*Keesee*, 1989; *Määttänen et al.*, 2005] is taken from *Seki and Hasegawa* [1983], who estimated the desorption energy from the wetting energy of water to $\alpha - \mathrm{SiO_2}$. Needless to say, this value might change considerably for different substrate materials and crystal modifications (crystalline or amorphous). As an example, reducing ΔF_{des} by 50% lowers the nucleation rate by seven orders of magnitude, which introduces a great uncertainty to the nucleation rate.

The desorption energy enters the equation of the nucleation rate because this energy is used to estimate the surface density of single water molecules on the ice nuclei, i.e. the monomer density $c_1 = p_{\mathrm{H_2O}}/(\nu(2\pi m_w kT)^{1/2}) \cdot \exp\left(\Delta F_{\mathrm{des}}/kT\right)$ [*Pruppacher and Klett*, 1997, Eq. 9-7]. According to this equation and for typical conditions of 130 K and a water vapor mixing ratio of 2 ppm at 87 km, the monomer concentration would be $c_1 = 3 \cdot 10^6$ cm^{-2}. Other studies, e.g. *Trainer et al.* [2009], used $c_1 = 1 \cdot 10^{15}$ cm^{-2}, which corresponds to the surface density of an ice monolayer. As c_1 squared contributes to the nucleation rate [*Pruppacher and Klett*, 1997], uncertainties in the monomer concentration have a large contribution to the uncertainty of J.

229 However, besides the uncertainty in the exact value of c_1, it is questionable whether
230 water molecules in general exist as monomers on the surface of MSP, as water molecules
231 have the ability to form hydrogen bonds with their neighbours. The absence of hydrogen
232 bonds can have two reasons [*Henderson*, 2002]: Firstly, kinetic constraints may prevent
233 water-water interactions (i.e., hydrogen bonds). Secondly, water-surface interactions may
234 be dominating and may thus be hindering water-water interactions. However, if the
235 water-surface interactions are too strong, the water will even be dissociated. *Henderson*
236 [2002] gives a detailed discussion of those different cases. They conclude that "monomeric
237 water is a rare state of water on most surfaces, with clustering and dissociation being the
238 predominate forms of adsorbed water" [*Henderson*, 2002]. If this is also valid for adsorbed
239 water on MSP, the currently assumed nucleation theory must be reconsidered, as it relies
240 on the assumption that the majority of water molecules exist as monomers, which then
241 form dimers, trimers and so forth until the critical radius is reached.

242 Finally, it should be mentioned here that an additional free charge on the surface of an
243 ice nuclei will also alter several nucleation properties. As charged MSP are not considered
244 in this study, we refer to the detailed discussion of *Gumbel and Megner* [2009] and *Megner*
245 *and Gumbel* [2009].

246 The foregoing discussion illustrates our lack of knowledge concerning the nucleation
247 process under mesospheric conditions. Some basic concepts may not be applicable to
248 meospheric conditions and many numerical values have not yet been determined in labo-
249 ratory experiments. Until these issues are resolved we have to rely on the currently used
250 classical nucleation theory and must be aware that the nucleation rate is highly uncer-

tain. The sensitivity of the nucleation rate to some of the above discussed parameters is visualized in Figure 1.

3. Model Setup

3.1. CARMA

CARMA, the Community Aerosol and Radiation Model for Atmospheres, is a microphysical model with a flexible setup, which can be applied to a variety of aerosol and cloud problems. The original one-dimensional CARMA code developed by *Turco et al.* [1979] and *Toon et al.* [1979] was later extended to three dimensions [*Toon et al.*, 1988] and adapted to mesospheric conditions [*Turco et al.*, 1982; *Jensen and Thomas*, 1989] for NLC studies (e.g., *Rapp et al.* [2002]; *Merkel et al.* [2009]; *Stevens et al.* [2010]; *Russell III et al.* [2010]; *Siskind et al.* [2011]; *Chandran et al.* [2012]). The CARMA model simulates three constituents: MSP, ice particles and water vapor. These constituents are able to interact via the following reactions: nucleation of MSP to form ice particles, deposition of water vapor onto ice particles for their growth, sublimation of ice particles with release of water vapor and in the case of total evaporation with release of MSP, and finally also coagulation of MSP and ice particles with themselves and with each other. An Eulerian transport scheme handles the transport of aerosols and water vapor due to background winds and eddy diffusion. In order to fulfill the continuity equation in a one-dimensional setup, a divergence correction is applied according to *Jensen and Thomas* [1989]: A divergent vertical flow is thereby compensated by horizontal advection from virtual neighbouring boxes with identical properties, bringing aerosol particles and water vapor into the considered gridbox (and vice versa for a convergent vertical flow).

The size distribution of aerosol particles is resolved in 40 size bins with mass doubling between adjacent bins, starting from minimal radii of 0.2 nm for MSP and 2 nm for ice particles. The model domain covers the altitude range from 72 km to 102 km in 120 equidistant levels of 250 m thickness. The time step is set to 100 s for all slow processes like transportation and coagulation. The fast microphysical processes nucleation and growth are calculated on shorter time scales, where the time step is adjusted according to the current microphysical conditions of each grid box.

We utilize the CARMA model in the version used by *Rapp and Thomas* [2006] with several advancements: (1) The background state of the mesopause region can either be described by climatological profiles as in the setup by *Rapp and Thomas* [2006] or with wave driven profiles taken from the KMCM, the Kühlungsborn Mechanistic general Circulation Model (see below). The KMCM profiles of temperature, density, pressure and wind are updated in CARMA every 600 s. (2) The dust profile has been updated according to the profile from the global and seasonal MSP model by *Megner et al.* [2008b] for July conditions at 68° N. The MSP model by *Megner et al.* [2008b] takes the meridional transport of MSP into account, which leads to significantly lower number densities, as the MSP are effectively transported away from the summer pole before growing to sizes relevant for nucleation. At the mesopause the resulting number density of MSP larger than 1 nm (which is a typical critical radius for climatological polar summer mesopause conditions) is 15 cm^{-3}, with strongly increasing number density towards smaller radii (100 cm^{-3} with radius larger than 0.8 nm and 2000 cm^{-3} with radius larger than 0.5 nm). The previously used MSP profile adopted from *Hunten et al.* [1980] is constant over the CARMA altitude range and has an MSP number density of 2650 cm^{-3} for particles larger

than 1 nm (5600 cm^{-3} for dust particles larger than 0.8 nm and 16300 cm^{-3} for particles larger than 0.5 nm). (3) Some minor changes in the code providing more consistency in the microphysical calculations are listed in the Appendix. As in the setup of *Rapp and Thomas* [2006] we operate CARMA in a one dimensional setup. This 1D setup is necessary in order to run the large number of sensitivity runs for this study in reasonable computation time.

3.2. Kühlungsborn Mechanistic general Circulation Model (KMCM)

The Kühlungsborn Mechanistic general Circulation Model (KMCM) is designed to explicitly model the gravity wave drag in the extratropical upper mesosphere. The turbulent diffusive damping of resolved waves (particularly gravity waves in the mesosphere/lower thermosphere) is self-consistently induced via vertical and horizontal diffusion coefficients, which depend on the Richardson number [*Becker and Burkhardt*, 2007]. The model is based on a dynamical core of standard spectral general circulation models [*Simmons and Burridge*, 1981] with truncation at total wavenumber 120, corresponding to a minimum horizontal wavelength resolved in the model of 330 km. The model comprises 190 hybrid levels from the surface to about 125 km altitude with a vertical spacing of about 600 m up to 105 km altitude. The complete model description can be found in *Becker* [2009]. It is important to note here that tides are not included in the KMCM data.

We use two weeks of KMCM data generated for July conditions. An overview over this data set is given in Figure 2, which shows the temperature and vertical wind fields used in this study. The mean profiles of this data set are shown in Figure 3 with the RMS values of the fluctuations indicated by the shaded area (corresponding to one standard deviation): Typical temperature fluctuations are on the order of 9 K and typical wind fluctuations

316 are on the order of 0.45 m/s with maximum amplitudes of up to 1.5 m/s. For comparison
317 the climatological profiles are included. Note that the climatological temperature profile
318 for July, which is also used in this study (see Section 4.2.1) and has been used in previous
319 studies (e.g., *Rapp et al.* [2002]; *Rapp and Thomas* [2006]), is colder than the mean KMCM
320 profile by about 5 K. The KMCM temperature cannot be simply shifted by this offset,
321 because the consistency with the wind, pressure and density field would then be lost.
322 However, the mean KMCM profile lies well within the range of expected temperature
323 profiles during the NLC season (cf. with temperature profiles for June and August). The
324 mean vertical wind from KMCM is directed upward with a mean velocity of only a few
325 cm/s which is similar to the values used in the climatological setup.

3.3. Setup of Sensitivity Experiments

326 As discussed in Section 2 several of the parameters determining the nucleation rate are
327 highly uncertain. This leads to possible nucleation rates that vary over several orders of
328 magnitude. We consider the effect of this uncertainty by performing sensitivity studies,
329 where the nucleation rate is varied over ± 10 orders of magnitude.

330 The desorption energy and surface tension are the two parameters with the greatest
331 influence on the nucleation rate, so that a variation of those two captures the range
332 of possible values. They both modify different limiting values: The desorption energy
333 occurs in the exponential term of the nucleation rate as one of the summands, so that the
334 uncertainty of this parameter can simply be implemented as a prefactor to the nucleation
335 rate. It thus only changes the order of magnitude of the nucleation rate J. This is
336 illustrated in Figure 1 where the nucleation rate for changed ΔF_{des} (red) is simply the
337 reference curve shifted along the y-axis. In contrast the surface tension modifies not only

the order of magnitude of J but also the critical radius r^*, indicated in Figure 1 with a shift along the x-axis. The rate of newly formed ice particles is determined by both parameters, by the order of magnitude of J and by the number of MSP that are possible ice nuclei, i.e. which are larger than r^*. Thus, varying the nucleation rate via the surface tension will have the effect that the individual influence of either shifting r^* or varying the order of magnitude of J cannot be separated from each other. We therefore restrict our study to a variation of the nucleation rate via a prefactor that accounts for the uncertainty of ΔF_{des}. For example, a prefactor of 10^7 corresponds to a value of ΔF_{des} that is increased by 50%. The uncertainty of the critical radius, and therefore also the uncertainty of the number density of available MSP, will be considered in additional simulations by changing the total MSP number density and its size distribution. With this approach, the effect of both parameters can be clearly distinguished. To be completely consistent with Equation 1 the prefactor should be temperature dependent. We neglect this temperature dependence because we expect the onset of nucleation to always occur around the same temperature, as J shows a very strong increase for decreasing temperatures (e.g. more than five orders of magnitude increase in J when going from 131 K to 130 K).

The expression for the nucleation rate in the model strictly follows Equation 1. MSP are considered as good ice nuclei so that the contact parameter is chosen to be $m = 0.95$. The mean jump distance is assumed to be $\bar{\delta} = 0.1$ nm, the vibration frequency $\nu = 10^{13}$ Hz, $\Delta F_{\mathrm{des}} = 2.9 \cdot 10^{-20}$ J and $\Delta F_{\mathrm{sd}} = 0.1 \Delta F_{\mathrm{des}}$. These are the values proposed by *Keesee* [1989].

Two different background profiles are used in this study to describe the atmospheric state: For our first set of simulations a climatological background is used with the mean

temperature profile in July derived from falling sphere measurements at 69° N by *Lübken* [1999] and the mean vertical wind from the model of *Berger and Zahn* [2002]. Following the suggestion of *Merkel et al.* [2009] and *Chandran et al.* [2012], the model is initialized in a warmer state to prevent unrealistic nucleation bursts in the first time step. Starting with a temperature offset of 12 K, the atmosphere is then subsequently cooled by 1 K/h. The final temperature profile is reached after 12 h and the model is run for another 48 h. Our second set of CARMA runs is based on KMCM background profiles for 69°N, 16°E. From the two week KMCM data set we choose six starting times (see vertical lines in Figure 2 (a)) for CARMA simulations with a duration of 48 h each. The different starting times are chosen to capture a variety of dynamical features. Common for all starting times is that we start the simulation in the warm phase of a wave, again to prevent unrealistic nucleation bursts in the first time step. This procedure with several shorter simulations is necessary, as CARMA cannot be run arbitrarily long in a one dimensional setup. The main reason is that on time scales greater than two days the ice particles are transported over significant distances by the meridional wind and should therefore experience changing background conditions, which would not be accounted for. The MSP size distribution is taken from *Megner et al.* [2008b] for 68°N. For some selected simulations the dust profile of *Hunten et al.* [1980] (as implemented by *Rapp and Thomas* [2006] without an altitude dependence) is used. These simulations with the profile of *Hunten et al.* [1980] are intended for conceptual studies or to facilitate the comparison with other modelling studies where the MSP are uniformly distributed over the complete altitude range.

In additional sensitivity runs we vary the background conditions. We add an altitude and time independent offset of −10 K, −5 K, −3 K, −1 K, and 1 K, scale the vertical

wind by a factor of 0.5 and multiply the MSP profile of *Megner et al.* [2008b] with the factors 100, 10, 0.1, 0.01, and 0.001.

4. Results

4.1. Mean Properties of Modelled NLC and Dependence on Nucleation Rate

The mean properties of NLC modelled under reference conditions with the KMCM background profiles are depicted in Figure 4. Panel (a) shows the mean number density and panel (b) the mean radius. The mean number density is roughly constant over the altitude range from 81 km to 88 km with 200 cm^{-3} to 300 cm^{-3} (dashed line). Limiting the modelled NLC to those which would be detectable in measurements (solid line), in this case applying the detection threshold of SOFIE (extinction coefficient greater than $2 \cdot 10^{-7}$ km^{-1} at 3.064 µm, *Hervig et al.* [2009a]), a commonly found altitude dependence is obtained, where the number density strongly increases with altitude [as in *Bardeen et al.*, 2010; *Hultgren and Gumbel*, 2014]. The difference can be explained by the corresponding profile of the mean particle size with small particles at high altitudes and larger ones below. The optical signal is extremely sensitive to the particle radius (scaling with power laws between r^6 and r^3 depending on observation wavelength). High clouds with small particles can only be detected when having large number densities. The applied detection limit therefore induces a bias towards larger number densities. The mean particle radius reaches its maximum value of 13 nm at 82 km. Compared to particles sizes retrieved from observations [e.g., *Hervig et al.*, 2009b; *Hultgren and Gumbel*, 2014; *Baumgarten et al.*, 2008], these particles remain comparatively small.

The radius of the ice particles is partly determined by the nucleation rate, as illustrated in Figure 5. Panel (a) presents NLC formed in the climatological background with

standard nucleation rate (top) and with a nucleation rate reduced by three orders of magnitude (bottom). Panel (b) presents NLC formed in the wave driven background, also for the standard nucleation rate (top) and for a nucleation rate reduced by five orders of magnitude (bottom). In both cases the particles grow to significantly larger radii if the nucleation rate is reduced. The maximum backscatter signal at 532 nm, a frequently used wavelength for lidar detection of NLC [e.g., *Baumgarten et al.*, 2008; *Thayer et al.*, 2003], is increased by more than 1000% upon reduction of J in the wave driven case. Thus the nucleation rate can make the difference between NLC which are detectable or not.

In order to understand the basic dependencies between ice particle number density, mean radius and backscatter signal we analyse the first set of CARMA simulations with climatological background conditions and the dust profile of *Hunten et al.* [1980]. This set of simulations provides an excellent framework to study the effects of varying nucleation rates, as no influence comes from varying nucleation altitudes as it would be the case when using the *Megner et al.* [2008b] profile or time dependent background conditions. Figure 6 gives an overview over the NLC properties after 36 h of simulation time (24 h after reaching the final background temperature) for nucleation rate prefactors between 10^{-10} and 10^{10}. The total ice particle number density n_{tot} at the altitude of the maximum backscatter coefficient is given in black and the mean radius r_{mean} in blue. The red curves show the maximum NLC backscatter coefficient β_{max} for light with a wavelength of $\lambda = 532$ nm. The different curves refer to the optical properties obtained for spheroids with axis ratios (AR) between between AR = 1/7 and AR = 7 [*Rapp et al.*, 2007; *Hervig et al.*, 2009b], the backscatter coefficients obtained for spheres are marked with crosses. The range of axis ratios is based on satellite observations reported by *Hervig et al.* [2009b]. Although the

majority of NLC detected by SOFIE has AR ≈ 2, NLC with lower ice mass density tend to be more aspherical (up to AR = 7). For calculating the optical properties we used the T-Matrix code by *Mishchenko and Travis* [1998]. The prefactor reflects a change of the desorption energy ΔF_{des}, which is indicated by the upper scale in Figure 6 for nucleation conditions at 130 K (e.g., a 50% increase of ΔF_{des} corresponds to a prefactor of 10^7).

Several basic dependencies can be directly inferred from Figure 6: In the low nucleation rate regime (prefactor less than 10^{-2}) a linear relationship is found between the nucleation rate prefactor and the total ice particle number density. For larger prefactors, n_{tot} reaches the limiting value of about 10^2 cm^{-3}. The smallest values for r_{mean} are reached in the large prefactor regime. In this regime the ice particle growth is limited by the available water vapor, which a large number of ice particles competes for. In the low prefactor regime the radius is limited by the growth time. In the relevant altitude range and for typical water vapor mixing ratios of a few ppm, the growth rate lies between 3 nm/h and 10 nm/h, which results in (unrealistically large) mean radii of about 130 nm after roughly 24 h of particle growth.

This first overview already shows that NLC with completely different properties can be modelled for the same background atmosphere by just changing the nucleation rate. However, not all of the scenarios lead to NLC properties which are commonly observed. We therefore compare the NLC parameters from our CARMA simulations with those derived from lidar measurements and we also briefly compare them with satellite measurements.

4.2. Comparison with Lidar Measurements

Baumgarten et al. [2008] present a summary of NLC properties (e.g. total number density and mean radius) for different NLC brightness classes from 8 years of lidar mea-

surements at ALOMAR (69° N, 16° E). This data set is used to benchmark our model results. In a first step we identify the brightness class (faint, weak, medium and strong NLC; *Fiedler et al.* [2003]) of the simulated NLC, considering axis ratios between 1/7 and 7. Then, we check whether the mean radius and number density fall within one standard deviation of the values given by *Baumgarten et al.* [2008, Table 3]. If this is the case we call it a 'match' and mark the corresponding nucleation rate prefactor in a color according to the brightness class (see Figures 7 and 8). This procedure is repeated for every time step of the simulation.

4.2.1. Simulation Results for Climatological Background

Figure 7 (a) depicts the results for climatological background conditions and both dust profiles. In the case of the *Hunten et al.* [1980] profile we find that the standard nucleation rate (prefactor 1) yields good results in producing NLC in all brightness classes (from faint to strong NLC) and with properties similar to those observed. NLC generated with higher nucleation rates (prefactor larger than 1) are also similar to observed NLC. In this prefactor regime the nucleation rate does not a have a significant influence on NLC properties, as shown in Figure 6. Reducing the nucleation rate by more than a factor of 10^{-2} prohibits matches in any brightness class. In the case of the *Megner et al.* [2008b] profile, the nucleation rate must be two to three orders of magnitude higher to compensate for the lower MSP number density. This is visible in the onset of 'realistic' NLC at prefactors larger than 10. MSP number densities differ by two to three orders of magnitude between the considered MSP-cases (see numbers in Section 3.1, but note that they are altitude dependent). Even though the lower MSP number densities in the profile of *Megner et al.* [2008b] can partly be compensated for by a higher nucleation rate

per particle, the final number of ice particles is nevertheless limited by the number of MSP. The low number density of ice particles allows them to grow to exceptionally (and unrealistically) large radii (130 nm and more) and become very bright. As a result, the combination of ice number density, mean radius and backscatter coefficient is not in the range of typical observations of *Baumgarten et al.* [2008]. Consequently no matches are found for medium and strong NLC with the dust profile of *Megner et al.* [2008b].

4.2.2. Simulation Results for Wave-Driven Background

Figure 7 (b) shows the same analysis as in (a) but with the wave driven background fields of the KMCM and for all six starting times of the CARMA simulations. The first point to note is that the prefactor range where 'realistic' NLC occur is strongly limited and centered around a prefactor of about 10^{-4} for the *Hunten et al.* [1980] profile and 10^{-1} for the *Megner et al.* [2008b] profile. As in the climatological case, the difference between the two dust profiles can be attributed to the different number densities of available MSP (i.e. MSP larger than r^*) which differ by about two to three orders of magnitude. Contrary to the results shown in Figure 7 (a), both dust profiles lead to matches in only the brightness classes of faint and weak NLC. Brighter clouds generally do not develop in these simulations with the reference KMCM background profile. This is a first indication that by going from the climatological background profiles to the wave driven profiles, new constraints arise since the NLC development is strongly determined by dynamics. As we will show later this is due to the wave-driven background fields, in particular due to waves in the vertical wind, which limits the growth time of the ice particles.

The sensitivity of our results to changing background conditions and varied MSP number densities is analysed in the following: We vary the MSP number density by multiplying

the original profile with the factors of 100, 10, 0.1, 0.01 and 0.001. Note that this can either reflect the general uncertainty of the MSP number density or the uncertainty of the critical radius. A reduction of the MSP number density thereby corresponds to a larger critical radius, and vice versa for an increase of the MSP number density. The temperature profile is varied by adding an altitude and time independent offset of -10 K, -5 K, -3 K, -1 K, and 1 K, reflecting, for example, the effect of planetary waves, tides or the seasonal variation. The sensitivity to the vertical wind variations is tested by multiplying the wind field with a factor of 0.5. Temperature and wind fields are changed independently of each other, so they do not necessarily represent a realistic state of the atmosphere. However, this setup allows to distinguish wind induced effects from temperature induced effects. These CARMA simulations are evaluated with the same method as described above. The results are presented in Figure 8.

From Figure 8 (a) we find that the nucleation rate range for which realistic NLC can be modelled is directly linked to the available MSP number density. An increase of the MSP number density by one order of magnitude shifts the matching nucleation rate prefactors by one order of magnitude towards lower prefactors. When the MSP number density is reduced by a factor of 0.1, NLC occur over a broad range of nucleation rate prefactors. Since even fewer MSP are present, the nucleation rate must generally be higher and the large nucleation rate rapidly depletes the available MSP. If this happens on time scales much smaller than typical dynamical time scales or typical time scales for particle growth, then the nucleation rate can be almost arbitrarily large without altering the NLC properties. For the lowest MSP number densities, none of the simulated NLC match the observations, because too few ice particles are generated to yield sufficiently bright NLC.

From the simulations with varied background temperature (b) we find that the prefactor range that leads to realistic NLC is less restricted for lower temperatures. We also find that the temperature has to be decreased by 3 K for medium NLC to develop and by 10 K for strong NLC.

Panel (c) shows the sensitivity to the vertical wind velocity. NLC brightness is greatly increased if the vertical wind is scaled by a factor of 0.5. Scaling the vertical wind retains the time intervals of upward and downward transport and simply increases or reduces the vertical distance travelled by the ice particles during one wave cycle. If the wind amplitude is reduced by only a factor of two, strong and medium NLC develop, whereas otherwise only medium and faint NLC occur. This increase in brightness can be explained by the particle trajectories which are shown in Figure 9. The trajectories start in the nucleation region and end when n_{tot} is below 0.01 cm^{-3}. Their position is determined by integrating the vertical velocity, i.e. the vertical wind velocity and sedimentation velocity based on the size bin with most particles. Panel (a) of Figure 9 shows NLC properties for the original wind field and Panel (b) for wind velocities reduced by a factor of two. The black lines represent characteristic trajectories. While in panel (b) the trajectories follow the up- and downward motion throughout several wave cycles, they are mostly limited to only one downward phase in the original wind field in Panel (a). Since the trajectories visualize the transport of the ice particles it becomes clear that a reduction of the vertical wind greatly enhances the ice particle lifetime. As a consequence, the ice particles grow to larger radii (middle row) and the backscatter coefficient increases (bottom row).

4.3. Comparison with Satellite Measurements

NLC properties have been extensively studied from space [e.g., *DeLand et al.*, 2006]. Sophisticated retrievals allow for the deduction of microphysical parameters such as the total number density of ice particles and their mean radius [e.g., *Thomas and McKay*, 1985; *von Savigny et al.*, 2004; *Karlsson and Gumbel*, 2005; *Hervig et al.*, 2009a]. The SOFIE instrument on the AIM satellite uses solar occultation measurements in the wavelength range from 0.3 µm to 5.3 µm to determine NLC properties as well as vertical profiles of temperature, water vapor and other trace gas mixing ratios [*Gordley et al.*, 2009]. Further measurements of mesospheric ice particle properties have recently been performed by the OSIRIS instrument on the Odin satellite [*Hultgren et al.*, 2013]. By applying a tomographic retrieval they are able to simultaneously determine horizontal and vertical profiles of ice particle properties. Under the assumption of a Gaussian size distribution where the width is directly inferred from the mean radius [*Baumgarten et al.*, 2010], *Hultgren and Gumbel* [2014] derive the number density, mean radius and ice mass density of NLC.

Hervig et al. [2009a, Fig. 17] depict their SOFIE NLC measurements in the $n_{\mathrm{tot}} - r_{\mathrm{mean}}$ plane, with all datapoints from the altitude of the maximum extinction coefficient. *Hultgren and Gumbel* [2014, Fig. 9] show a similar plot with their $n_{\mathrm{tot}} - r_{\mathrm{mean}}$ measurements, but with datapoints from the complete vertical profile. We chose to visualize the properties of our simulated NLC in the same way to enable a qualitative comparison with the two satellite data sets. Figure 10 (a) shows the CARMA results at the altitude of maximum backscatter coefficient, color coded by the nucleation rate prefactor. The gray box in the background marks the values reported by *Hervig et al.* [2009a]. In Figure 10

(b) the simulated ice particle properties for all altitudes are shown, again color coded by the nucleation rate prefactor. Here, the gray box marks the range of values reported by *Hultgren and Gumbel* [2014]. The hatched area in this panel denotes the area where measurement are sparse in their data set. In these figures the data of all KMCM simulations with the MSP profile of *Megner et al.* [2008b] in the reference setup and those with varied background temperatures are combined, as those possibly present realistic states of the atmosphere. The data set is limited to those points with an ice mass density greater than 0.1 $\mathrm{ng\,m^{-3}}$, which is the detection limit of SOFIE [*Hervig et al.*, 2009a].

We find that the best coverage of the parameter space seen by the two satellites is achieved with CARMA simulations using reduced nucleation rates (dark purple data points). The large particle radii which are detected by the satellites (up to 70 nm and 120 nm for SOFIE and OSIRIS respectively) are only generated in CARMA runs with nucleation rate prefactors lower than 10^{-2}. However, not the whole observed parameter space is covered by our simulations. In particular, the range where the satellite data extends to larger number densities and simultaneously to larger radii is not covered by the model runs. The NLC situated in this range are characterised by large ice mass densities, which are not reached in the model.

5. Discussion

The nucleation rate is a critical factor which determines the properties of mesospheric ice particles. By changing the nucleation rate, we are able to generate NLC with notably different characteristics. When using a MSP background profile with rather numerous MSP (the profile from *Hunten et al.* [1980]) the nucleation rate must be reduced significantly in order to model NLC that resemble those seen by observations. The comparison

584 with lidar measurements [*Baumgarten et al.*, 2008] yields the best agreement if the nu-
585 cleation rate is reduced by four to five orders of magnitude compared to the reference
586 case described by Equation 1. As the nucleation rate is defined by the nucleation rate
587 per particle times the MSP number density, the above mentioned reduction of the nu-
588 cleation rate can partly be compensated by a lower number density of MSP, such as in
589 the MSP profile by *Megner et al.* [2008b]. The comparison with satellite observations of
590 NLC [*Hervig et al.*, 2009a; *Hultgren and Gumbel*, 2014] yields the best agreement if the
591 nucleation rate is reduced by two orders of magnitude or more for both dust profiles.

592 The theoretically expected inverse relationship between nucleation rate per particle and
593 MSP number density is supported by our simulations: Increasing the MSP number density
594 by one order of magnitude requires the nucleation rate prefactor to be decreased by one
595 order of magnitude to yield equivalent NLC (see Figure 8). This inverse relationship
596 holds as long as there are enough MSP available, i.e. the limiting factor is not the
597 availability of MSP but the nucleation rate. If the availability of MSP is the limiting
598 factor, the nucleation rate can be arbitrarily large in our simulations without affecting
599 NLC properties.

5.1. Comparison with 'Minimal Impact' Hypothesis by *Megner* [2011]

600 The backscatter signal B should be roughly proportional to $N \cdot r^6$ based on the rea-
601 sonable assumption that mesospheric ice particles act as Rayleigh scatterers in the visi-
602 ble wavelength range and beyond. Expressing the radius r via the ice mass M_{ice} yields
603 $B \propto M_{\mathrm{ice}}^2/N$. The backscatter signal should thus vary with ice number density N and
604 should therefore depend on the number density of initial ice nuclei, i.e. the MSP num-
605 ber density. This relationship has previously been investigated by *Megner* [2011]. Using

the CARMA model she varied the number density of 1 nm-sized MSP from 1 cm^{-3} to 10^5 cm^{-3} and analyzed the resulting NLC properties. Unexpectedly, she found B and M_{ice} to be almost independent of the initial ice nuclei number density N.

Our set of simulations includes sensitivity runs with different MSP number densities, which we use to test the $B \propto M_{ice}^2/N$ relationship. The set of simulations with the *Hunten et al.* [1980] profile and varied number densities are set up similar to the simulations by *Megner* [2011]: (1) no altitude dependence of the MSP profile and (2) with a MSP number density that ranges from about 2 cm^{-3} (MSP x 0.001) to $2 \cdot 10^5$ cm^{-3} (MSP x 100) for MSP larger than 1 nm, covering the complete range of MSP number densities that has been analysed by *Megner* [2011]. Following her analysis we consider column integrated variables, so that B is the integrated albedo and M_{ice} is the ice water column. However, our resulting NLC properties show several differences: In Figure 11 (a) we present the time series of the ice water column M_{ice}, which is more sensitive to the initial number of MSP than in the analysis of *Megner* [2011, Fig. 2 (a)] (note the logarithmic scale in our plot). Increasing the MSP number density mainly shifts the curves of M_{ice} to larger values. The behaviour of the integrated albedo B in panel (b) is more complex due to the nonlinearity of the cloud development process. We therefore test the relationship by plotting M_{ice}^2/B in panel (c), which should be proportional to N. This is roughly the case, as the different curves are separated by about one order of magnitude, reflecting the one order of magnitude difference in the underlying MSP number density. To illustrate this dependence more clearly the time averaged values for M_{ice}^2/B are shown versus MSP number densities in panel (d). We find an almost linear dependence, supporting the $B \propto M_{ice}^2/N$ relationship. Only the CARMA run 'MSP x 100' deviates significantly from

this relationship. In this simulation the NLC development is limited by the available water vapor. Due to the very large number density of MSP, a large number of ice particles is formed which rapidly depletes the available water vapor. It is thus not available at later time steps, leading to a gradual decrease of B in the 'MSP x 100' run. The conclusion to be drawn from this analysis is that our simulations follow the simple relationship of $B \propto M_{\mathrm{ice}}^2/N$, at least as long as the available water vapor is not the limiting factor.

How can the difference to the simulations of *Megner* [2011] be explained? *Megner* [2011] used wave-perturbed temperature fields to drive the model, but did not use (except for one case) the corresponding wind fields. Instead, the ice particles experienced a time-constant up-draft due to the mean vertical wind. Hence, the only way for ice particles to reach lower altitudes where they can grow effectively ('growth region') is by Eddy diffusion. This is also the case when *Megner* [2011] used the wave-perturbed wind fields, as the assumed vertical wind velocities were smaller than the turbulent velocities associated with the vertical Eddy diffusion coefficient [*Lübken*, 1997]. As a result, the simulated properties in *Megner* [2011] are independent of the initial number of ice particles. In our simulations the dominant process for vertical transport is the vertical wind, because the turbulent velocities and sedimentation velocities are comparable to or smaller than our wave-perturbed wind velocities. As seen for example in Figure 5 the whole particle population is transported downward with the wave-perturbed wind after nucleation. The total ice particle number density is roughly unchanged between the nucleation region and growth region. Therefore, all nucleated particles do contribute to the brightness of the cloud. Hence we find a clear relationship between initial MSP number density or nucleation conditions in general and the observed NLC properties.

5.2. Discussion of Sensitivities

652 The evaluation results presented in Figure 8 (b) emphasise the importance of the back-
653 ground temperature. The first point to note is that in an atmosphere with lower back-
654 ground temperature, the development of realistic NLC is less sensitive to the nucleation
655 rate. The second point is that medium and strong NLC only develop if the temperature
656 is reduced by at least 3 K and 10 K, respectively. This result is consistent with different
657 interpretations of the temperature offset implemented in our simulations: First of all,
658 the mean KMCM temperature has a warm bias of about 5 K compared to the coldest
659 temperatures measured at ALOMAR by *Lübken* [1999] with the falling spheres technique
660 (see Figure 3). Nevertheless, the mean KMCM profile lies well in the range of temper-
661 atures measured within the NLC season. Our result that NLC get brighter in a colder
662 environment is consistent with the observed seasonal variation. The brightest NLC are
663 detected at the peak of the season around 25 days after solstice (mid of July) [*Fiedler*
664 *et al.*, 2009]. This coincides with the minimum temperatures of the climatology by *Lübken*
665 [1999]. However, a reduction of 5 K in the model is not enough to yield strong NLC. This
666 implies that for the development of strong NLC an additional forcing is necessary. The
667 temperature offset we implemented in the simulations can reflect large scale temperature
668 perturbations with long periods and large vertical wavelengths, such as planetary waves
669 or tides. It has been shown in various studies that both have major influence on NLC.
670 *Fiedler et al.* [2005] conclude from the mean diurnal variation of NLC that occurrence,
671 brightness and altitude of NLC are significantly controlled by tides. Planetary waves
672 are known to modulate NLC occurrence and brightness [e.g., *Kirkwood and Stebel*, 2003;
673 *Merkel et al.*, 2003]. It was shown by *Merkel et al.* [2008] that the brightness of NLC

674 is almost anticorrelated to the temperature perturbations induced by planetary waves.
675 They find that the maximum amplitude of temperature perturbations is relatively small
676 (2 K - 3.5 K) but has a significant effect on NLC brightness. We find similar indications
677 in our CARMA simulations, where a reduction of the background temperature by 3 K
678 increases the NLC brightness from weak to medium NLC (see Figure 8(b)). *Liu et al.*
679 [2015] find similar temperature amplitudes and a high anticorrelation to NLC ice water
680 content. For a temperature decrease of 3 K, they measure an ice water content increase
681 between 5 g/km^2 and 30 g/km^2 (see their Fig. 5). Our simulations show a similar re-
682 sponse: A reduction of the background temperature of 3 K leads to an increase of the
683 ice water content between 17 g/km^2 and 34 g/km^2. We consider this as support for the
684 interpretation of the temperature offset in terms of planetary wave perturbations.

685 Besides the nucleation conditions and background temperatures, the vertical wind at the
686 mesopause is one of the key parameters that affect NLC properties in our simulations. The
687 magnitude and direction of the vertical wind determines the residence time of ice particles
688 in the supersaturated altitude range. As the cold phase of a wave is typically followed by
689 a downwind phase, freshly nucleated ice particles are subsequently transported to lower
690 altitudes by the background wind, which is much faster than the additional downward
691 sedimentation. Ice particles which are transported below the supersaturated region will
692 evaporate rapidly. If the ice particles survive the downwind phase they can experience
693 another full wave cycle with the following upwind phase, which extends their lifetime
694 significantly. Whether the ice particles survive the downwind phase or not depends on
695 the wind amplitude, the period of the wave and the vertical extent of the supersaturated
696 region. Since the lifetime determines the maximum size and therefore also the brightness

of the cloud, it is crucial to check whether our KMCM wind amplitudes are realistic or not.

First of all it is important to stress that the mesopause region is characterized by highly variable vertical wind velocities. This large variability and also the amplitude of the vertical wind have been measured by various instruments and reported in numerous studies. Typical vertical wind amplitudes measured by the EISCAT (European Incoherent Scatter) radar range from ±2 m/s to ±6 m/s [*Hoppe and Hansen*, 1988; *Hoppe and Fritts*, 1995; *Mitchell and Howells*, 1998; *Rapp and Hoppe*, 2006], vertical wind variances range from 5 m^2/s^2 to 15 m^2/s^2 [*Fritts et al.*, 1990; *Strelnikova and Rapp*, 2011]. Vertical wind variances measured by the mobile SOUSY (SOUnding SYstem) radar are on the order of 2 m^2/s^2 to 3 m^2/s^2 [*Rüster and Reid*, 1990]. MAARSY, the Middle Atmosphere Alomar Radar System, regularly detects vertical wind amplitudes of 5 m/s [*Stober et al.*, 2013]. From chaff foil cloud experiments wind amplitudes of ±4 m/s to ±6 m/s have been deduced [*Widdel*, 1987]. Vertical wind velocities determined from the Doppler shift of the OH emission line, measured with a Michelson interferometer by *Bhattacharya and Gerrard* [2010], reveal daily mean velocities (over an 8 h window) of 0 m/s to ±10 m/s with daily standard deviations of 7 m/s to 14 m/s. Iron lidar measurements reported by *Höffner and Lautenbach* [2009] show vertical wind amplitudes of ±4 m/s. The KMCM vertical wind velocities are at maximum 1.5 m/s, the variance is about 0.25 m^2/s^2, as indicated by the standard deviation in Figure 3. Compared to the measurements listed above, the KMCM wind amplitudes are significantly smaller. However, the important question is, on which time scales dominant upward or downward motions persist, as the short time scales (5 min to 30 min) contribute the most to the total vertical wind variance [e.g. *Rüster and*

Reid, 1990; *Fritts et al.*, 1990; *Strelnikova and Rapp*, 2011]. The MAARSY measurements reveal large scale variations of the wind field, where phases of up and down-welling last up to several hours [*Stober et al.*, 2013]. These wind fields are comparable to our KMCM field (Figure 2), except for the additional superimposed fluctuations on shorter time scales found in the radar measurements. Similar characteristics are present in the wind fields reported by *Höffner and Lautenbach* [2009] and to some lesser extent by *Mitchell and Howells* [1998].

From a theoretical perspective, the perturbations of temperature $\hat{T}$ and vertical wind $\hat{w}$ which are induced by gravity waves are related via the polarization relation [e.g., *Holton*, 2004; *Geller and Gong*, 2010; *Fritts et al.*, 2014]

$$\hat{w} = \frac{\mathrm{i}g\omega}{N^2}\frac{\hat{T}}{T_0} \tag{4}$$

with background temperature T_0, gravitational acceleration g, Brunt-Väisälä frequency N and angular frequency of the gravity wave ω. For typical conditions ($T_0 = 130$ K, $N = 0.02$ s^{-1}, $g = 9.81$ m/s^{-2}) a 10 K temperature amplitude [*Rapp et al.*, 2002] is associated with a vertical wind amplitude of $\hat{w} = 0.83$ m/s or 0.33 m/s for a 4 h or 10 h wave, respectively. In KMCM typical temperature fluctuations at the mesopause are $\hat{T} = 9$ K with wind fluctuations of $\hat{w} = 0.45$ m/s (see Figure 3). This agrees very well with the theoretically expected values for waves with periods on the order of 6 h. For a detailed study on the applicability of the polarization relations to mesospheric conditions, see *Placke et al.* [2013].

Megner et al. [2009] report NLC at exceptionally high altitudes, which were detected by rocket photometers. The peculiarity of this NLC was that it consisted of large particles

(effective radius of 50 nm), which does not comply with the conventional picture of ice particles which grow as they sediment to lower altitudes. They concluded that strong upwelling was necessary for the explanation of their observation. NLC that existed below the altitude range of supersaturation have been found by *Christensen* [2015, Paper E], who combined tomographic measurements of temperature, water vapor and NLC from the Odin satellite. They found that these ice particles were not able to reach those low altitudes only by sedimentation, but rather needed downward vertical wind velocities on the order of 1 m/s to 3 m/s. Both these studies are examples where observations can only be explained by strong vertical winds.

Instead of directly comparing the vertical wind, we can also compare the downward progression rate of NLC. Early studies as those from *Langer* [1995] report downward progression rates between 1.8 km/h and 2.6 km/h. *Kaifler et al.* [2013b] analyze the progression rate depending on the duration of the NLC. They find a mean downward progression rate of 0.3 km/h, which comprises upward and downward motions of NLC equally. Focusing only on the downward motion (e.g. in their Fig. 3) we identify the predominant rates to range between 1.3 km/h and 2.3 km/h. A typical NLC from the CARMA model, as for example the ice particles which become visible after 25 h in Figure 5, has a downward progression rate of about 1.8 km/h. This value lies well in the range of the measured downward progression rates.

The following four points summarize the discussion of the vertical wind velocities: (1) Radar observations of the vertical wind velocity show large amplitudes on a regular basis. (2) Vertical wind perturbations in KMCM agree well with those associated with typical temperature perturbations at the summer mesopause. (3) NLC measure-

ments have been reported which can only be explained by the presence of large vertical winds. (4) The downward motion of the modelled NLC, which is mainly determined by the vertical wind, lies well within the range of lidar measurements.

These comparisons are only singular reference points, but make us confident that the vertical wind velocities are within a reasonable range. To which extent the vertical wind influences the development of NLC shows the comparison with the work of *Kiliani et al.* [2013]. They studied the temporal evolution of NLC using the Leibniz-Institute Middle Atmosphere (LIMA) model with the Lagrangian ice transport model LIMA/ICE. Their ice particles reside at approximately their nucleation altitude for more than two days, before they progress downward at the sedimentation rate of ~ 0.2 km/h. This is in sharp contrast to our simulations where the ice particles survive only a few wave cycles and the vertical motion is almost solely controlled by the vertical wind (see Figure 9). This can be attributed to the significantly smaller vertical velocities in the LIMA model, which range from -0.2 m/s to 0.15 m/s. This is roughly the range reported by *Stevens et al.* [2010] for monthly mean values of the vertical wind using a mesospheric data assimilation system. As seen above, instantaneous wind amplitudes are much higher than these average values.

The main question of this study was to what extent the properties of mesospheric ice particles are governed by the nucleation rate. We find that the nucleation rate is indeed a crucial factor, but nevertheless 'suitable' dynamical conditions are a prerequisite for the development of detectable NLC. Suitable dynamical conditions are those where ice particles are able to remain in the supersaturated altitude region until they grow to detectable sizes. This is for example given in the climatological background fields, where the mean vertical wind is directed upward and counteracts sedimentation. However, in

the wave driven simulations it is not the mean vertical wind which determines the NLC development. It is rather the variability of the vertical wind, which imposes additional constraints on the growth of mesospheric ice particles. The high sensitivity to the vertical velocity is one of the conclusions to be drawn from Figure 8 (c) and the trajectories presented in Figure 9.

When using wave driven background profiles the exact calculation of the microphysical processes becomes essential. The duration of ice particle growth is limited and the assumption that an existing supersaturation will be considerably depleted is no longer applicable. Thus, when going from NLC simulations with rather slowly varying climatological background conditions to more realistic ones, new limitations arise which challenge our current understanding of the microphysical development of NLC [e.g., *Rapp and Thomas*, 2006; *Hultgren and Gumbel*, 2014].

It must be kept in mind, that the relevant parameter that we varied is the rate of newly formed ice particles. We achieved this by varying the nucleation rate per particle. Similar results can be achieved by varying the ice nuclei number density. We find from our simulations with the MSP profile of *Hunten et al.* [1980] that the nucleation rate must be reduced by four to five orders of magnitude to yield realistic NLC. This statement is in a limited range equivalent to saying that in order to model realistic NLC the MSP number density must be lower than in the profile of *Hunten et al.* [1980]. This interpretation of our results fits well to the results of *Megner et al.* [2008b], who find that under the influence of meridional transport the number density of MSP is significantly lower than in the distribution of *Hunten et al.* [1980]. As their profile yields only about 10 MSP per cm^3 that are larger than 1 nm, *Megner et al.* [2008a] pose the challenging question, whether

MSP can in general provide enough ice nuclei to explain the phenomenon of electron bite-outs [e.g., *Ulwick et al.*, 1988]. Strong electron bite-outs occur occasionally in the vicinity of PMSE [*Blix et al.*, 2003; *Li and Rapp*, 2013] and require ice number densities on the order of 10^3 cm^{-3} to be explained [*Reid*, 1990]. *Megner et al.* [2008a] argue that a nucleus which carries a charge has a significantly reduced critical radius (or even no critical radius at all). Thus, a larger fraction of the MSP population would be available as ice nuclei, which could solve the dilemma of too low ice nuclei number densities. We find in our simulations with the profile of *Megner et al.* [2008b] that ice number densities on the order of several 10^3 cm^{-3} and up to 10^5 cm^{-3} are easily reached (see Figure 10). This is because the wave induced temperature fluctuations lower the critical radius dramatically and allow for a large fraction of the MSP size distribution to nucleate. We therefore conclude that it is not a necessary prerequisite that the ice nuclei are charged for the explanation of large ice number densities. Instead, a temperature induced lowering of the critical radius is a possible alternative explanation. This, however, does not question the importance of considering charged MSP in modelling mesospheric ice particles.

6. Summary

In this paper we show how the properties of mesospheric ice particles are governed by the nucleation rate. We set up the microphysical model CARMA with a variable nucleation rate ($\pm$10 orders of magnitude compared to standard assumptions), different MSP profiles (by *Megner et al.* [2008b] and by *Hunten et al.* [1980]) and with climatological as well as with wave driven background profiles.

NLC modelled in a background atmosphere with wave driven perturbations of temperature and vertical wind have significantly different properties than those modelled for

832 climatological conditions. The reason is that the mechanisms which limit the growth of
833 these ice particles are different: In climatological backgrounds, the ice particles can con-
834 sume the available water vapor until the supersaturation is depleted. Until that point is
835 reached, the only limitation is sedimentation, which is partly compensated by the prevail-
836 ing upward vertical wind. This results in rather long particle lifetimes between several
837 hours and days. In wave driven backgrounds the lifetime is significantly shorter. The ice
838 particles commonly survive only a few wave cycles, often even only one. The times where
839 ice particles can nucleate and grow are therefore strongly limited. We find that due to this
840 limitation the characteristic microphysical time scales gain in importance and determine
841 whether the ice particles grow to detectable sizes or not. This requires exact microphys-
842 ical modelling of nucleation and subsequent growth. However, our understanding of the
843 nucleation process under mesospheric conditions is poor, concerning the exact nucleation
844 pathway as well as the parameters which determine the nucleation rate quantitatively.
845 Since the nucleation rate determines one of the critical microphysical time scales, NLC
846 properties strongly depend on the nucleation conditions.

847 In order for NLC to grow to detectable sizes and have similar properties as those de-
848 tected by lidar and satellite measurements, the nucleation rate must be reduced compared
849 to standard assumptions of the classical nucleation theory. In case of numerous MSP as
850 in the dust profile of *Hunten et al.* [1980] the nucleation rate must be reduced by four
851 to five orders of magnitude to best match the properties reported from lidar observations
852 [*Baumgarten et al.*, 2008]. Given fewer MSP as in the profile of *Megner et al.* [2008b],
853 standard assumptions lead to fairly realistic properties. We generally find that the more
854 MSP are available (e.g., because the critical radius is small), the lower the nucleation

rate per particle must be for modelling realistic NLC. Satellite observations and modelled NLC agree best when the nucleation rate is reduced by two orders of magnitude or more. In particular large particle radii up to 100 nm only develop in simulations with reduced nucleation rates. Larger nucleation rates produce larger number densities of ice particles, which tend to result in very dim NLC and which often remain below the detection threshold of optical instruments.

In general, low nucleation rates can mean that either the nucleation rate per particle must be small or that only few ice nuclei are present in the polar summer mesopause. Low MSP number densities have been predicted by global MSP models [*Megner et al.*, 2008b; *Bardeen et al.*, 2008], which led to the question whether these few MSP could provide enough ice nuclei for the observed mesospheric phenomena. We find that a low MSP number density (or low nucleation rate per particle) is not a hindrance of NLC development, it is rather a prerequisite.

The nucleation rate and the wave driven background conditions at the mesopause are equally critical for the formation of NLC: The nucleation rate determines the number density of ice particles, while the dynamical state of the background atmosphere governs the subsequent particle growth. Especially the vertical wind limits the lifetime of mesospheric ice particles and should therefore receive special consideration in forthcoming NLC modelling studies. From our simulations we further find that an additional cooling as for example caused by tides or planetary waves is necessary for the formation of bright NLC.

In order to reduce the uncertainty in the nucleation rate laboratory experiments under mesospheric conditions are vitally important. The experimental setup recently presented

by *Duft et al.* [2015] has promising capabilities and will hopefully shed some light on the exact microphysical processes.

Appendix A: Changes in CARMA

Changes made in the CARMA code as compared to the version 2.1 used by *Rapp and Thomas* [2006]:

1. A sign error in the parametrization of the surface energy was corrected to agree with *Hale and Plummer* [1974]. As seen in Figure 1 the surface tension plays a crucial role for the nucleation rate. With the corrected parametrization, σ is reduced by about 25%. This shifts the critical radius from 1.5 nm to 1.1 nm (background conditions of 130 K, water vapor mixing ratio of 2 ppm and 0.3 Pa).

2. The nucleation rate given by *Asmus et al.* [2014] is implemented, which allows the particle temperature to be different from the ambient gas temperature. For the case that the particle temperature is equal to the temperature of the surrounding gas the nucleation rate simplifies to the one given by *Keesee* [1989]. The original CARMA version by *Rapp and Thomas* [2006] included the nucleation rate by *Jensen* [1989], with a monomer concentration $c_1 = 10^{28}$ cm^{-2} (compare with the now implemented c_1 value given in Section 2). This yielded nucleation rates that were higher by roughly 20 orders of magnitude. However, this does not mean, that the generated ice number densities were also larger by 20 orders of magnitude, but rather that the MSP number density was almost instantaneously depleted. As shown in Figure 6 the ice number density reaches a limiting value for larger nucleation rates and the NLC properties are not considerably altered by a further increase of J.

3. The prefactor `gro` of the ice particle growth rate is updated every time step to account for changing background conditions.

4. The density of the ice cores, which consist of meteoric dust material, is set to `rhoelem(3)`=2 g/cm^3 in order to match the density of the MSP in the model. This itself does not change the results significantly. However, if `rhoelem(3)` is changed further adjustments have to be made as otherwise the growthrate is reduced by a factor of two: In the subroutine setupbins.f the variable `rhop3(ixyz,ibin,ig)` has to be set to `rhoelem(ienconc(ig))` instead of `rhoelem(ie)`.

5. To ensure that the water vapor concentration stays positive, a retry mechanism similar to the one suggested by *Bardeen et al.* [2013] was implemented. The basic idea is that the microphysical calculations are repeated with reduced time step if the gas concentration `gc` turns negative. This procedure is repeated until `gc` remains positive throughout the complete time step. If this would require the number of substeps to be larger than `maxsubsteps`, the microphysics are skipped from the substep on before `gc` would turn negative.

Acknowledgments. H. W. was supported by DFG Grant MicroIce RA 1400/3-1. All data used to achieve the presented results can be requested from the corresponding author at henrike.wilms@dlr.de

References

Asmus, H., H. Wilms, B. Strelnikov, and M. Rapp (2014), On the heterogeneous nucleation of mesospheric ice on meteoric smoke particles: Microphysical modeling, *J. Atmos. Sol. Terr. Phy.*, *118*, 180 – 189, doi:10.1016/j.jastp.2014.03.009.

Bardeen, C. G., O. B. Toon, E. J. Jensen, D. R. Marsh, and V. L. Harvey (2008), Numerical simulations of the three-dimensional distribution of meteoric dust in the mesosphere and upper stratosphere, *J. Geophys. Res.*, *113*, D17,202, doi:10.1029/2007JD009515.

Bardeen, C. G., O. B. Toon, E. J. Jensen, M. E. Hervig, C. E. Randall, S. Benze, D. R. Marsh, and A. Merkel (2010), Numerical simulations of the three-dimensional distribution of polar mesospheric clouds and comparisons with Cloud Imaging and Particle Size (CIPS) experiment and the Solar Occultation For Ice Experiment (SOFIE) observations, *J. Geophys. Res.*, *115*, D1024, doi:10.1029/2009JD012451.

Bardeen, C. G., A. Gettelman, E. J. Jensen, A. Heymsfield, A. J. Conley, J. Delanoë, M. Deng, and O. B. Toon (2013), Improved cirrus simulations in a general circulation model using CARMA sectional microphysics, *J. Geophys. Res.*, *118*, 11,679 – 11,697, doi:10.1002/2013JD020193.

Baumgarten, G., and D. C. Fritts (2014), Quantifying Kelvin-Helmholtz instability dynamics observed in noctilucent clouds: 1. Methods and observations, *J. Geophys. Res.*, *119*, 9324–9337, doi:10.1002/2014JD021832.

Baumgarten, G., J. Fiedler, F.-J. Lübken, and G. v. Cossart (2008), Particle properties and water content of noctilucent clouds and their interannual variation, *J. Geophys. Res.*, *113*(D6), doi:10.1029/2007JD008884.

Baumgarten, G., J. Fiedler, and M. Rapp (2010), On microphysical processes of Noctilucent Clouds (NLC): Observations and modeling of mean and width of the particle size-distribution, *J. Atmos. Chem.*, *10*, 6661–6668, doi:10.5194/acp-10-6661-2010.

Baumgarten, G., A. Chandran, J. Fiedler, P. Hoffmann, N. Kaifler, J. Lumpe, A. Merkel, C. E. Randall, D. Rusch, and G. Thomas (2012), On the horizontal and temporal

942 structure of noctilucent clouds as observed by satellite and lidar at ALOMAR (69N),
943 *Geophys. Res. Lett.*, *39*, L01,803, doi:10.1029/2011GL049935.

944 Becker, E. (2009), Sensitivity of the Upper Mesosphere to the Lorenz Energy
945 Cycle of the Troposphere, *Journal of Atmospheric Sciences*, *66*, 647–666, doi:
946 10.1175/2008JAS2735.1.

947 Becker, E., and U. Burkhardt (2007), Nonlinear Horizontal Diffusion for GCMs, *Mon.*
948 *Wea. Rev.*, *135*(4), 1439–1454, doi:10.1175/mwr3348.1.

949 Berger, U., and U. v. Zahn (2002), Icy particles in the summer mesopause region: Three-
950 dimensional modeling of their environment and two-dimensional modeling of their trans-
951 port, *J. Geophys. Res.*, *107*(A11), doi:10.1029/2001JA000316.

952 Bhattacharya, Y., and A. J. Gerrard (2010), Wintertime mesopause region vertical winds
953 from Resolute Bay, *J. Geophys. Res.*, *115*, doi:10.1029/2010jd014113.

954 Blix, T., M. Rapp, and F.-J. Lübken (2003), Relations between small scale electron num-
955 ber density fluctuations, radar backscatter, and charged aerosol particles, *J. Geophys.*
956 *Res.*, *108*(D8), 8450, doi:10.1029/2002JD002430.

957 Chandran, A., D. W. Rusch, S. E. Palo, G. E. Thomas, and M. J. Taylor (2009), Grav-
958 ity wave observations in the summertime polar mesosphere from Cloud Imaging and
959 Particle Size (CIPS) experiment on the AIM spacecraft, *J. Atmos. Sol. Terr. Phy.*, *71*,
960 392–400, doi:10.1016/j.jastp.2008.09.041.

961 Chandran, A., W. Rusch, G. E. Thomas, S. E. Palo, G. Baumgarten, E. J. Jensen, and
962 A. W. Merkel (2012), Atmospheric gravity wave effects on polar mesospheric clouds:
963 A comparison of numerical simulations from CARMA 2D with AIM observations, *J.*
964 *Geophys. Res.*, *117*, D20,104, doi:10.1029/2012JD017794.

965 Christensen, O. M. (2015), *Mesospheric measurements using microwave spectroscopy*,
966 Doktorsavhandlingar vid Chalmers tekniska högskola. Ny serie, no: 3916, Institutionen
967 för rymd- och geovetenskap, Global miljömätteknik och modellering, Chalmers tekniska
968 högskola,, 189.

969 DeLand, M. T., E. P. Shettle, G. E. Thomas, and J. J. Olivero (2006), A quarter-century
970 of satellite polar mesospheric cloud observations, *J. Atmos. Sol. Terr. Phy.*, *68*(1), 9–29,
971 doi:10.1016/j.jastp.2005.08.003.

972 Duft, D., M. Nachbar, M. Eritt, and T. Leisner (2015), A Linear Trap for Studying the
973 Interaction of Nanoparticles with Supersaturated Vapors, *Aerosol Sci. Technol.*, *49*(9),
974 682–690, doi:10.1080/02786826.2015.1063583.

975 Eidhammer, T., and O. Havnes (2001), Size dependence of the mesospheric dust temper-
976 ature And its influence on the noctilucent clouds and polar mesosphere summer echo
977 phenomena, *J. Geophys. Res.*, *106*(A11), 24,831–24,841.

978 Fiedler, J., G. Baumgarten, and G. von Cossart (2003), Noctilucent clouds above ALO-
979 MAR between 1997 and 2001: Occurrence and properties, *J. Geophys. Res.*, *108(D8)*,
980 8453, doi:10.1029/2002JD002419.

981 Fiedler, J., G. Baumgarten, and G. von Cossart (2005), Mean diurnal variations of noc-
982 tilucent clouds during 7 years of lidar observations at ALOMAR, *Ann. Geophys.*, *23*,
983 1175 – 1181, doi:10.5194/angeo-23-1175-2005.

984 Fiedler, J., G. Baumgarten, and F.-J. Lübken (2009), NLC observations during one
985 solar cycle above ALOMAR, *J. Atmos. Sol. Terr. Phy.*, *71*(3-4), 424 – 433, doi:
986 10.1016/j.jastp.2008.11.010.

987 Fiocco, G., G. Grams, and G. Visconti (1975), Equilibrium temperatures of small particles
988 in the Earth's upper atmosphere (50–110 km), *J. Atmos. Terr. Phys.*, *37*(10), 1327–
989 1337.

990 Fletcher, N. H. (1958), Size Effect in Heterogeneous Nucleation, *J. Chem. Phys.*, *29*(3),
991 572–576.

992 Fletcher, N. H. (1959), On ice-crystal production by aerosol particles, *J. Meteor.*, *16*(2),
993 173–180.

994 Fritts, D. C., U.-P. Hoppe, and B. Inhester (1990), A study of the vertical motion field
995 near the high-latitude summer mesopause during MAC/SINE, *Journal of Atmospheric*
996 *and Terrestrial Physics*, *52*(10), 927 – 938, doi:10.1016/0021-9169(90)90025-I.

997 Fritts, D. C., P.-D. Pautet, K. Bossert, M. J. Taylor, B. P. Williams, H. Iimura, T. Yuan,
998 N. J. Mitchell, and G. Stober (2014), Quantifying gravity wave momentum fluxes with
999 Mesosphere Temperature Mappers and correlative instrumentation, *Journal of Geo-*
1000 *physical Research*, *119*, 13,583–13,603, doi:10.1002/2014jd022150.

1001 Geller, M. A., and J. Gong (2010), Gravity wave kinetic, potential, and vertical fluctua-
1002 tion energies as indicators of different frequency gravity waves, *J. Geophys. Res.*, *115*,
1003 D11,111, doi:10.1029/2009JD012266.

1004 Gordley, L. L., M. E. Hervig, C. Fish, J. M. Russell III, S. Bailey, J. Cook, S. Hansen,
1005 A. Shumway, G. Paxton, L. Deaver, T. Marshall, J. Burton, B. Magill, C. Brown,
1006 E. Thompson, and J. Kempc (2009), The solar occulatation for ice experiment, *J.*
1007 *Atmos. Sol. Terr. Phy.*, *71*, 300–315.

1008 Gumbel, J., and L. Megner (2009), Charged meteoric smoke as ice nuclei in the meso-
1009 sphere: Part 1 - A review of basic concepts , *Journal of Atmospheric and Solar-*

Terrestrial Physics, *71*(12), 1225 – 1235, doi:10.1016/j.jastp.2009.04.012.

Gumbel, J., and G. Witt (2002), Cluster ions and ice particle nucleation: Positive feedback at the summer mesopause, *Geophys. Res. Lett.*, *29*(16), doi:10.1029/2002GL015146.

Hale, B. N., and P. L. M. Plummer (1974), Molecular model for ice clusters in a supersaturated vapor, *J. Chem. Phys.*, *61*, 4012 – 4019, doi:10.1063/1.1681694.

Henderson, M. A. (2002), The interaction of water with solid surfaces: fundamental aspects revisited, *Surface Science Reports*, *46*, 1 – 308, doi:10.1016/S0167-5729(01)00020-6.

Hervig, M. E., L. L. Gordley, M. H. Stevens, J. M. Russell III, S. M. Bailey, and G. Baumgarten (2009a), Interpretation of SOFIE PMC measurements: Cloud identification and derivation of mass density, particle shape, and particle size, *J. Atmos. Sol. Terr. Phy.*, *71*, 316–330, doi:10.1016/j.jastp.2008.07.009.

Hervig, M. E., L. L. Gordley, J. M. Russell III, and S. M. Bailey (2009b), SOFIE PMC observations during the northern summer of 2007, *J. Atmos. Sol. Terr. Phy.*, *71*, 331 – 339, doi:10.1016/j.jastp.2008.08.010.

Hervig, M. E., L. E. Deaver, C. G. Bardeen, J. M. Russell III, S. M. Bailey, and L. L. Gordley (2012), The content and composition of meteoric smoke in mesospheric ice particles from SOFIE observations, *J. Atmos. Sol. Terr. Phy.*, *84-85*, 1–6, doi:10.1016/j.jastp.2012.04.005.

Höffner, J., and J. Lautenbach (2009), Daylight measurements of mesopause temperature and vertical wind with the mobile scanning iron lidar, *Optics Letters*, *34*, 1351 – 1353, doi:10.1364/OL.34.001351.

1032 Holton, J. R. (2004), *An Introduction to Dynamic Meteorology*, International Geophysics
1033 Series, 4 ed., Elsevier Academic Press.

1034 Hoppe, U.-P., and D. C. Fritts (1995), High-resolution measurements of vertical velocity
1035 with the European incoherent scatter VHF radar 1. Motion field characteristics and
1036 measurement bias, *J. Geophys. Res.*, *100*(D8), 16,813 – 16,825.

1037 Hoppe, U.-P., and T. L. Hansen (1988), studies of vertical mmotion in the upper meso-
1038 sphere using EISCAT UHF radar, *Annales Geophysicae*, *6*(2), 181–186.

1039 Hultgren, K., and J. Gumbel (2014), Tomographic and spectral views on the lifecycle of
1040 polar mesospheric clouds from Odin/OSIRIS, *J. Geophys. Res.*, *119*(24), 14,129–14,143,
1041 doi:10.1002/2014JD022435.

1042 Hultgren, K., J. Gumbel, D. Degenstein, A. Bourassa, N. Lloyd, and J. Stegman (2013),
1043 First simultaneous retrievals of horizontal and vertical structures of Polar Mesospheric
1044 Clouds from Odin/OSIRIS tomography, *Journal of Atmospheric and Solar-Terrestrial*
1045 *Physics*, *104*, 213 – 223, doi:10.1016/j.jastp.2013.06.013.

1046 Hunten, D. M., R. P. Turco, and O. B. Toon (1980), Smoke and Dust Particles of Meteoric
1047 Origin in the Mesosphere and Stratosphere, *J. Atmos. Sci.*, *37*(6), 1342–1357.

1048 Jensen, E., and G. E. Thomas (1989), On the diurnal Variation of Noctilucent Clouds, *J.*
1049 *Geophys. Res.*, *94*(D12), 14,693–14,702.

1050 Jensen, E. J. (1989), A numerical model of polar mesospheric cloud formation and evolu-
1051 tion, Ph.D. thesis, University of Colorado.

1052 Kaifler, N., G. Baumgarten, J. Fiedler, and F.-J. Lübken (2013a), Quantification of waves
1053 in lidar observations of noctilucent clouds at scales from seconds to minutes, *Atmos.*
1054 *Chem. Phys.*, *13*, 7397–7429, doi:10.5194/acp-13-11757-2013.

Kaifler, N., G. Baumgarten, A. R. Klekociuk, S. P. Alexander, J. Fiedler, and F.-J. Lübken (2013b), Small scale structures of NLC observed by lidar at 69° N/69° S and their possible relation to gravity waves, *J. Atmos. Sol. Terr. Phy.*, *104*, 244–252, doi: 10.1016/j.jastp.2013.01.004.

Karlsson, B., and J. Gumbel (2005), Challenges in the limb retrieval of noctilucent cloud properties from Odin/OSIRIS, *Adv. Space Res.*, *36*(5), 935–942, doi: 10.1016/j.asr.2005.04.074.

Keesee, R. G. (1989), Nucleation and Particle Formation in the Upper Atmosphere, *J. Geophys. Res.*, *94*(D12), 14,683–14,692.

Kiliani, J., G. Baumgarten, F.-J. Lübken, U. Berger, and P. Hoffmann (2013), Temporal and spatial characteristics of the formation of strong noctilucent clouds, *J. Atmos. Sol. Terr. Phy.*, *104*, 151–166, doi:10.1016/j.jastp.2013.01.005.

Kirkwood, S., and K. Stebel (2003), Influence of planetary waves on noctilucent cloud occurrence over NW Europe, *J. Geophys. Res.*, *108*, 8440, doi:10.1029/2002JD002356.

Langer, M. (1995), Lidarbeobachtungen von leuchtenden Nachtwolken, Ph.D. thesis, Bonn University.

Lee, J. K., F. F. Abraham, and G. M. Pound (1973), On the validity of the capillarity approximation in the rate theory of homogeneous nucleation, *Surf. Sci.*, *34*, 745–758, doi:10.1016/0039-6028(73)90041-1.

Li, Q., and M. Rapp (2013), {PMSE} observations with the {EISCAT} vhf- and uhf-radars: Ice particles and their effect on ambient electron densities, *Journal of Atmospheric and Solar-Terrestrial Physics*, *104*, 270 – 276, doi:10.1016/j.jastp.2012.10.015.

1077 Liu, X., J. Yue, J. Xu, W. Yuan, J. M. Russell III, and M. E. Hervig (2015), Five-day waves
1078 in polar stratosphere and mesosphere temperature and mesospheric ice water measured
1079 by SOFIE/AIM, *J. Geophys. Res.*, doi:10.1002/2015JD023119, 2015JD023119.

1080 Lübken, F.-J. (1997), Seasonal variation of turbulent energy dissipation rates at high
1081 latitudes as determined by in situ measurements of neutral density fluctuations, *J.*
1082 *Geophys. Res.*, *102*, 13,441–13,456.

1083 Lübken, F.-J. (1999), Thermal structure of the Arctic summer mesosphere, *J. Geophys.*
1084 *Res.*, *104*, 9135 – 9149.

1085 Määttänen, A., H. Vehkamäki, A. Lauri, S. Merikallio, J. Kauhanen, H. Savijärvi, and
1086 M. Kulmala (2005), Nucleation studies in the Martian atmosphere, *J. Geophys. Res.*,
1087 *110*, E02,002, doi:10.1029/2004JE002308.

1088 Megner, L. (2011), Minimal impact of condensation nuclei characteristics on observ-
1089 able Mesospheric ice properties, *J. Atmos. Sol. Terr. Phy.*, *73*, 2184 – 2191, doi:
1090 10.1016/j.jastp.2010.08.006.

1091 Megner, L., and J. Gumbel (2009), Charged meteoric particles as ice nuclei in the meso-
1092 sphere: Part 2: A feasibility study, *J. Atmos. Sol. Terr. Phy.*, *71*(12), 1236 – 1244,
1093 doi:10.1016/j.jastp.2009.05.002.

1094 Megner, L., J. Gumbel, M. Rapp, and D. Siskind (2008a), Reduced meteoric smoke par-
1095 ticle density at the summer pole - Implications for mesospheric ice particle nucleation,
1096 *Adv. Space Res.*, *41*, 41–49, doi:10.1016/j.asr.2007.09.006.

1097 Megner, L., D. E. Siskind, M. Rapp, and J. Gumbel (2008b), Global and temporal distri-
1098 bution of meteoric smoke: A two-dimensional simulation study, *J. Geophys. Res.*, *113*,
1099 D03,202, doi:10.1029/2007JD009054.

1100 Megner, L., M. Khaplanov, G. Baumgarten, J. Gumbel, J. Stegman, B. Strelnikov, and
1101 S. Robertson (2009), Large mesospheric ice particles at exceptionally high altitudes,
1102 *Ann. Geophys.*, *27*(3), 943–951, doi:10.5194/angeo-27-943-2009.

1103 Merkel, A. W., G. E. Thomas, S. E. Palo, and S. M. Bailey (2003), Observations of the
1104 5-day planetary wave in PMC measurements from the Student Nitric Oxide Explorer
1105 Satellite, *Geophys. Res. Lett.*, *30*, 1196–1199.

1106 Merkel, A. W., R. R. Garcia, S. M. Bailey, and J. M. Russell III (2008), Observational
1107 studies of planetary waves in PMCs and mesospheric temperature measured by SNOE
1108 and SABER, *J. Geophys. Res.*, *113*, D14,202, doi:10.1029/2007JD009396.

1109 Merkel, A. W., D. R. Marsh, A. Gettelman, and E. J. Jensen (2009), On the relationship of
1110 polar mesospheric cloud ice water content, particle radius and mesospheric temperature
1111 and its use in multi-dimensional models, *Atmos. Chem. Phys.*, *9*, 8889–8901.

1112 Mishchenko, M. I., and L. D. Travis (1998), Capabilities and limitations of a current
1113 FORTRAN implementation of the T-matrix method for randomly oriented, rotationally
1114 symmetric scatterers, *J. Quant. Spectrosc. Radiat. Transfer*, *60*(3), 309 – 324.

1115 Mitchell, N. J., and V. S. C. Howells (1998), Vertical velocities associated with gravity
1116 waves measured in the mesosphere and lower thermosphere with the EISCAT VHF
1117 radar, *Ann. Geophys.*, *16*(10), 1367–1379, doi:10.1007/s00585-998-1367-0.

1118 Murray, B. J., and E. J. Jensen (2010), Homogeneous nucleation of amorphous solid water
1119 particles in the upper mesosphere, *J. Atmos. Sol. Terr. Phy.*, *72*(1), 51–61.

1120 Pautet, P.-D., J. Stegman, C. M. Wrasse, K. Nielsen, H. Takahashi, M. J. Taylor, K. W.
1121 Hoppel, and S. D. Eckermann (2011), Analysis of gravity waves structures visible
1122 in noctilucent cloud images, *J. Atmos. Sol. Terr. Phy.*, *73*(14-15), 2082–2090, doi:

1123 10.1016/j.jastp.2010.06.001.

1124 Placke, M., P. Hoffmann, M. Gerding, E. Becker, and M. Rapp (2013), Testing linear
1125 gravity wave theory with simultaneous wind and temperature data from the mesosphere,
1126 *J. Atmos. Sol. Terr. Phy.*, *93*, 57–69, doi:10.1016/j.jastp.2012.11.012.

1127 Plane, J. M. C. (2000), The role of sodium bicarbonate in the nucleation of noctilucent
1128 clouds, *Ann. Geophys.*, *18*, 807–814.

1129 Pruppacher, H. R., and J. D. Klett (1997), *Microphysics of clouds and precipitation*, 2
1130 ed., Kluwer Academic Publishers, Dordrecht and Boston.

1131 Rapp, M., and U.-P. Hoppe (2006), A reconsideration of spectral width measurements in
1132 PMSE with EISCAT, *Adv. Space Res.*, *38*, 2408–2412, doi:10.1016/j.asr.2004.12.029.

1133 Rapp, M., and G. E. Thomas (2006), Modeling the microphysics of mesospheric ice par-
1134 ticles: Assessment of current capabilities and basic sensitivities, *J. Atmos. Sol. Terr.*
1135 *Phy.*, *68*(7), 715–744, doi:10.1016/j.jastp.2005.10.015.

1136 Rapp, M., F.-J. Lübken, A. Müllemann, G. E. Thomas, and E. J. Jensen (2002), Small-
1137 scale temperature variations in the vicinity of NLC: Experimental and model results,
1138 *J. Geophys. Res.*, *107*(D19), 4392, doi:10.1029/2001JD001241.

1139 Rapp, M., G. E. Thomas, and G. Baumgarten (2007), Spectral properties of mesospheric
1140 ice clouds: Evidence for nonspherical particles, *J. Geophys. Res.*, *112*, D03,211, doi:
1141 10.1029/2006JD007322.

1142 Reid, G. C. (1990), Ice particles and electron 'bite-outs' at the summer po-
1143 lar mesopause, *Journal of Geophysical Research*, *95*(D9), 13,891–13,896, doi:
1144 10.1029/JD095iD09p13891.

Roddy, A. F. (1984), The role of meteoric particles in noctilucent clouds, *Irish Astronomical Journal*, *16*, 194 – 202.

Rong, P. P., J. Yue, J. M. Russell III, J. D. Lumpe, J. Gong, D. L. Wu, and C. E. Randall (2015), Horizontal winds derived from the polar mesospheric cloud images as observed by the CIPS instrument on the AIM satellite, *Journal of Geophysical Research*, *120*(11), 5564–5584, doi:10.1002/2014JD022813.

Russell III, J. M., P. Rong, S. M. Bailey, M. E. Hervig, and S. V. Petelina (2010), Relationship between the summer mesopause and polar mesospheric cloud heights, *J. Geophys. Res.*, *115*, D16,209, doi:10.1029/2010JD013852.

Rüster, R., and I. M. Reid (1990), VHF Radar Observations of the Dynamics of the Summer Polar Mesopause Region, *Journal of Geophysical Research*, *95*(D7), 10,005–10,016, doi:10.1029/JD095iD07p10005.

Saunders, R. W., and J. M. C. Plane (2006), A laboratory study of meteor smoke analogues: Composition, optical properties and growth kinetics, *J. Atmos. Sol. Terr. Phy.*, *68*, 2182–2202.

Seki, J., and H. Hasegawa (1983), The heterogeneous condensation of interstellar ice grains, *Astrophysics and Space Science*, *94*(1), 177–189.

Simmons, A. J., and D. M. Burridge (1981), An Energy and Angular-Momentum Conserving Vertical Finite-Difference Scheme and Hybrid Vertical Coordinates, *Mon. Wea. Rev.*, *109*(4), 758–766, doi:10.1175/1520-0493(1981)109¡0758:AEAAMC¿2.0.CO;2.

Siskind, D. E., M. H. Stevens, M. Hervig, F. Sassi, K. Hoppel, C. R. Englert, and A. J. Kochenash (2011), Consequences of recent Southern Hemisphere winter variability on polar mesospheric clouds, *Journal of Atmospheric and Solar-Terrestrial Physics*, *73*(13),

2013 – 2021, doi:10.1016/j.jastp.2011.06.014.

Stevens, M. H., D. E. Siskind, S. D. Eckermann, L. Coy, J. P. McCormack, C. R. Englert, K. W. Hoppel, K. Nielsen, A. J. Kochenash, M. E. Hervig, C. E. Randall, J. Lumpe, S. M. Bailey, M. Rapp, and P. Hoffmann (2010), Tidally induced variations of polar mesospheric cloud altitudes and ice water content using a data assimilation system, *Journal of Geophysical Research*, *115*(D18), doi:10.1029/2009JD013225.

Stober, G., S. Sommer, M. Rapp, and R. Latteck (2013), Investigation of gravity waves using horizontally resolved radial velocity measurements, *Atmospheric Measurement Techniques*, *6*, 2893–2905, doi:10.5194/amt-6-2893-2013.

Strelnikova, I., and M. Rapp (2011), Majority of PMSE spectral widths at UHF and VHF are compatible with a single scattering mechanism, *J. Atmos. Sol. Terr. Phy.*, *73*, 2142–2152, doi:10.1016/j.jastp.2010.11.025.

Sugiyama, T. (1994), Ion-recombination nucleation and growth of ice particles in noctilucent clouds, *J. Geophys. Res.*, *99*(A3), 3915–3929, doi:10.1029/93JA02822.

Thayer, J. P., M. Rapp, A. J. Gerrard, E. Gudmundsson, and T. J. Kane (2003), Gravity-wave influences on Arctic mesospheric clouds as determined by a Rayleigh lidar at Sondrestrom, Greenland, *J. Geophys. Res.*, *108(D8)*, 8449, doi:10.1029/2002JD002363.

Thomas, G. E. (1991), Mesospheric clouds and the physics of the mesopause region, *Rev. Geophys.*, *29*(4), 553, doi:10.1029/91RG01604.

Thomas, G. E., and C. P. McKay (1985), On the mean particle size and water content of polar mesospheric clouds, *Planet. Space Sci.*, *33*(10), 1209–1224, doi:10.1016/0032-0633(85)90077-7.

1190 Tolman, R. C. (1949), The Effect of Droplet Size on Surface Tension, *J. Chem. Phys.*, *17*,
1191 333, doi:10.1063/1.1747247.

1192 Toon, O. B., R. P. Turco, P. Hamill, C. S. Kiang, and R. C. Whitten (1979), A one-
1193 dimensional model describing aerosol formation and evolution in the stratosphere:
1194 II. Sensitivity studies and comparison with observations, *J. Atmos. Sci.*, *36*(4), 718–736,
1195 doi:10.1175/1520-0469(1979)036<0718:AODMDA>2.0.CO;2.

1196 Toon, O. B., R. P. Turco, D. Westphal, R. Malone, and M. Liu (1988), A multidimensional
1197 model for aerosols: Description of computational analogs, *J. Atmos. Sci.*, *45*(15), 2123–
1198 2143, doi:10.1175/1520-0469(1988)045¡2123:AMMFAD¿2.0.CO;2.

1199 Trainer, M. G., O. B. Toon, and M. A. Tolbert (2009), Measurements of Depositional Ice
1200 Nucleation on Insoluble Substrates at Low Temperatures: Implications for Earth and
1201 Mars, *J. Phys. Chem*, *113*, 2036 – 2040, doi:10.1021/jp805140p.

1202 Turco, R. P., P. Hamill, O. B. Toon, R. C. Whitten, and C. S. Kiang (1979), A one-
1203 dimensional model describing aerosol formation and evolution in the stratosphere:
1204 I. Physical processes and mathematical analogs, *J. Atmos. Sci.*, *36*(4), 699–717, doi:
1205 10.1175/1520-0469(1979)036<0699:AODMDA>2.0.CO;2.

1206 Turco, R. P., O. B. Toon, R. C. Whitten, R. G. Keesee, and D. Hollenbach (1982),
1207 Noctilucent clouds: Simulation studies of their genesis, properties and global influences,
1208 *Planet. Space Sci.*, *30*(11), 1147–1181, doi:10.1016/0032-0633(82)90126-X.

1209 Ulwick, J. C., K. D. Baker, M. C. Kelley, B. B. Balsley, and W. L. Ecklund
1210 (1988), Comparison of simultaneous MST radar and electron density probe mea-
1211 surements during STATE, *Journal of Geophysical Research*, *93*, 6989–7000, doi:
1212 10.1029/JD093iD06p06989.

Vehkamäki, H., A. Määttänen, A. Lauri, I. Napari, and M. Kulmala (2007), Technical Note: The heterogeneous Zeldovich factor, *Atmos. Chem. Phys.*, *7*, 309–313, doi: 10.5194/acp-7-309-2007.

von Savigny, C., A. Kokhanovsky, H. Bovensmann, K.-U. Eichmann, J. Kaiser, S. Noël, A. Rozanov, J. Skupin, and J. Burrows (2004), NLC detection and particle size determination: first results from SCIAMACHY on ENVISAT, *Adv. Space Res.*, *34*(4), 851–856, doi:10.1016/j.asr.2003.05.050.

Vonnegut, B. (1947), The Nucleation of Ice Formation by Silver Iodine, *J. Appl. Phys.*, *18*(7), 593 – 595, doi:10.1063/1.1697813.

Widdel, H.-U. (1987), Vertical movements in the middle atmosphere derived from foil cloud experiments, *J. Atmos. Terr. Phys.*, *49*(7-8), 723–731, doi:10.1016/0021-9169(87)90015-8.

Witt, G. (1962), Height, structure and displacements of noctilucent clouds, *Tellus Series A*, *14*(1), 1–18, doi:10.1111/j.2153-3490.1962.tb00115.x.

Witt, G. (1969), The Nature of Noctilucent Clouds, *Space Research*, *9*, 157–169.

Wood, S. E. (1999), Nucleation and growth of CO2 ice crystals in the Martian atmosphere, Ph.D. thesis, Dept. of Earth and Space Sciences, University of California, Los Angeles.

Zeldovich, Y. B. (1942), On the theory of formation of a new phase. Cavitation, *Zh. Eksp. Teor. Fiz.*, *12*, 525.

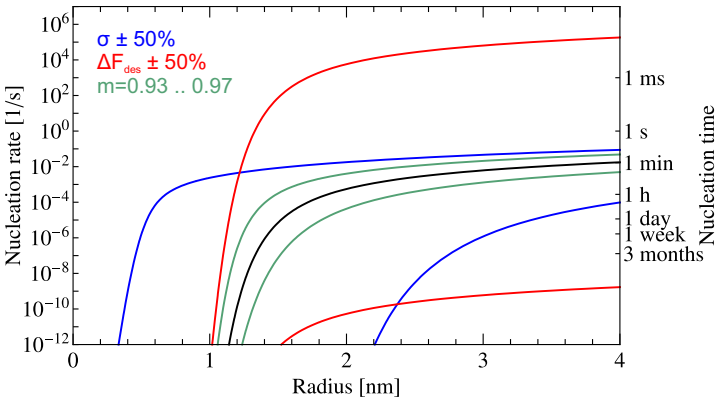

Figure 1. Nucleation rate per particle of radius r for typical mesopause conditions (black). The time to nucleate one particle is shown on the right hand axis. The sensitivity of the nucleation rate is demonstrated by increasing and reducing the surface tension σ (blue) and the desorption energy ΔF_{des} (red) by $\pm 50\%$. The contact parameter m is varied from 0.93 to 0.97 (green). The nucleation rates are calculated for a background temperature of 130 K and a water vapor mixing ratio of 2 ppm at 0.3 Pa background pressure.

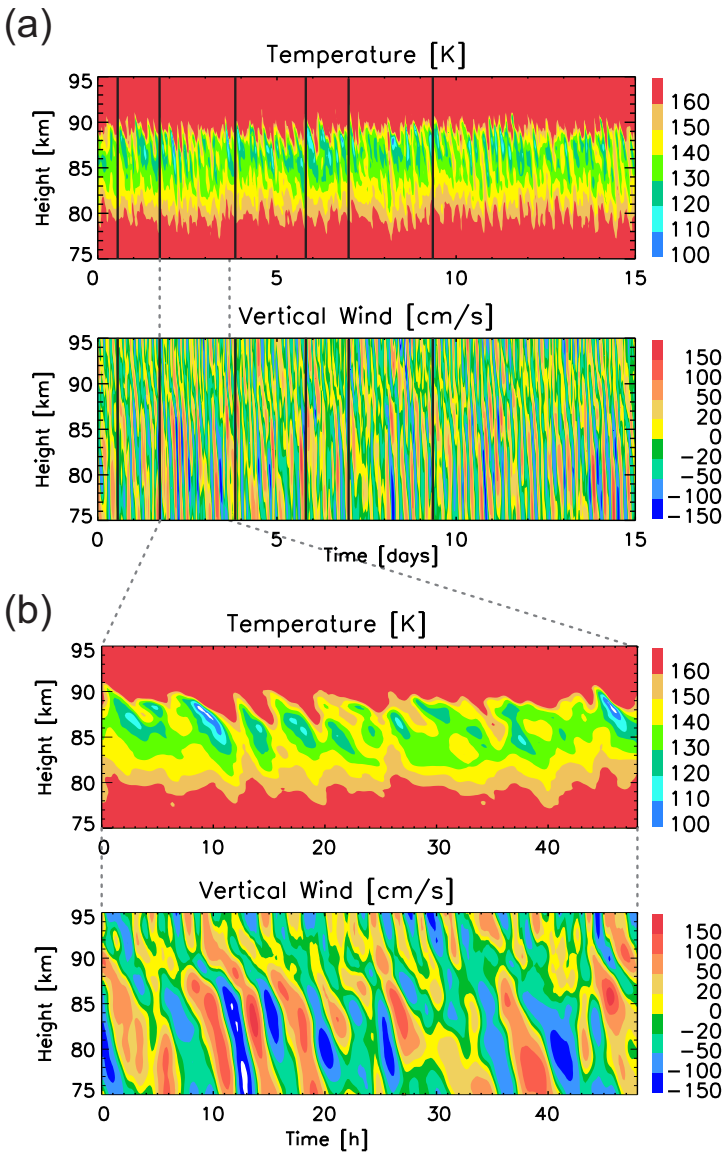

Figure 2. (a) KMCM time series of temperature and vertical wind velocity. Vertical lines indicate starting times of CARMA simulations. (b) One of the six background profiles used in this study.

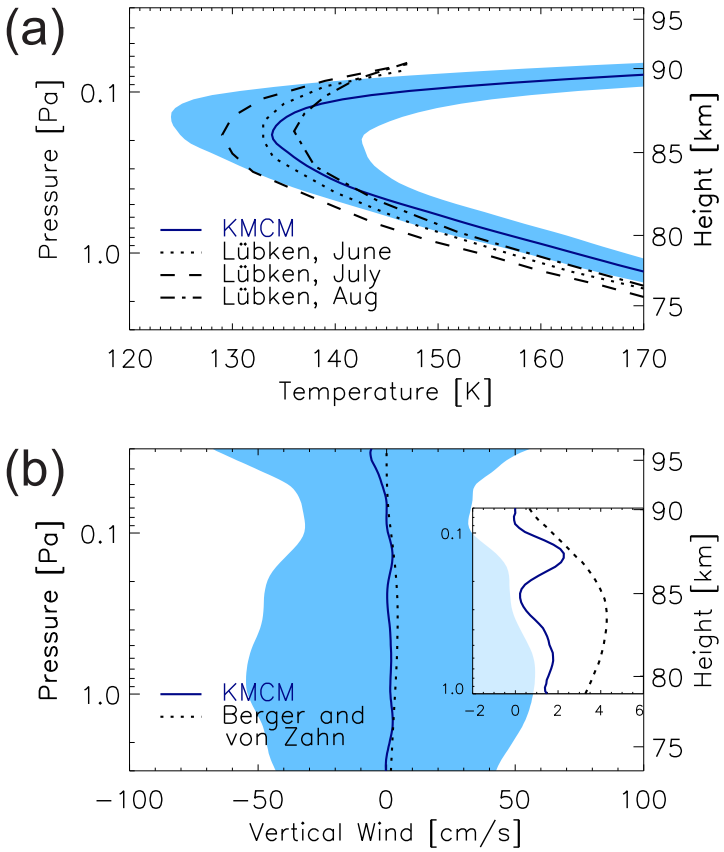

Figure 3. Mean profiles of (a) temperature and (b) vertical wind from KMCM. The shaded area corresponds to one standard deviation. For comparison, the climatological temperature profiles from falling sphere measurements in June, July and August [*Lübken*, 1999] are shown in (a) and modelled mean vertical winds from *Berger and Zahn* [2002] in (b). The pressure altitude conversion is based on the KMCM data, it differs slightly for the *Lübken* [1999] profiles.

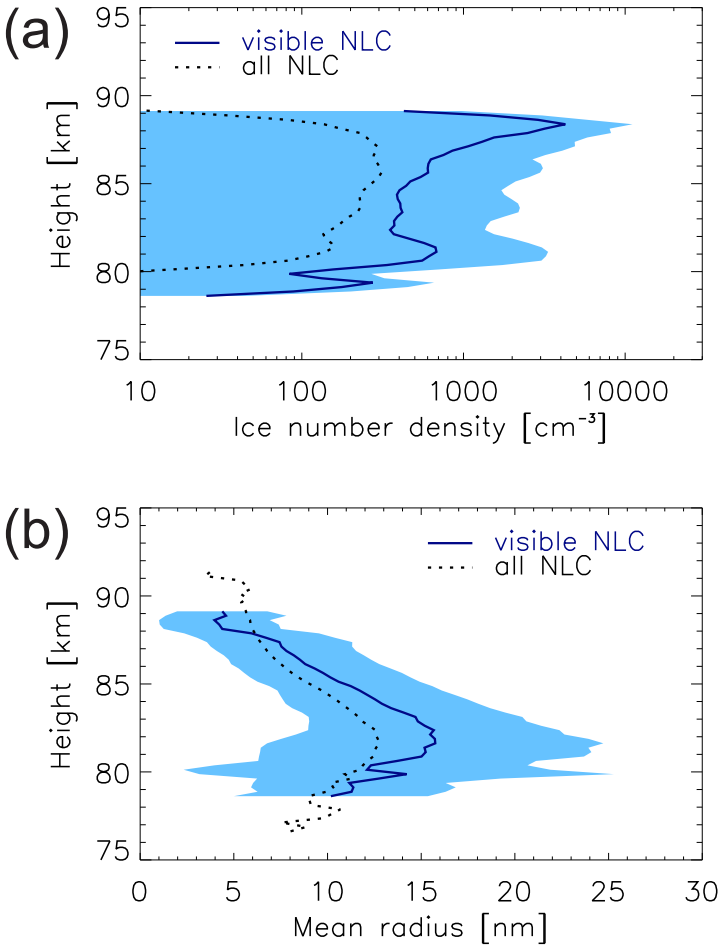

Figure 4. Mean properties of simulated NLC: (a) ice particle number density and (b) mean radius. The dashed line includes all simulated NLC and the solid line only those visible to SOFIE. The shaded area corresponds to one standard deviation of the visible NLC. The wave driven simulations with reference nucleation rate and the MSP profile of *Megner et al.* [2008b] have been averaged for these plots.

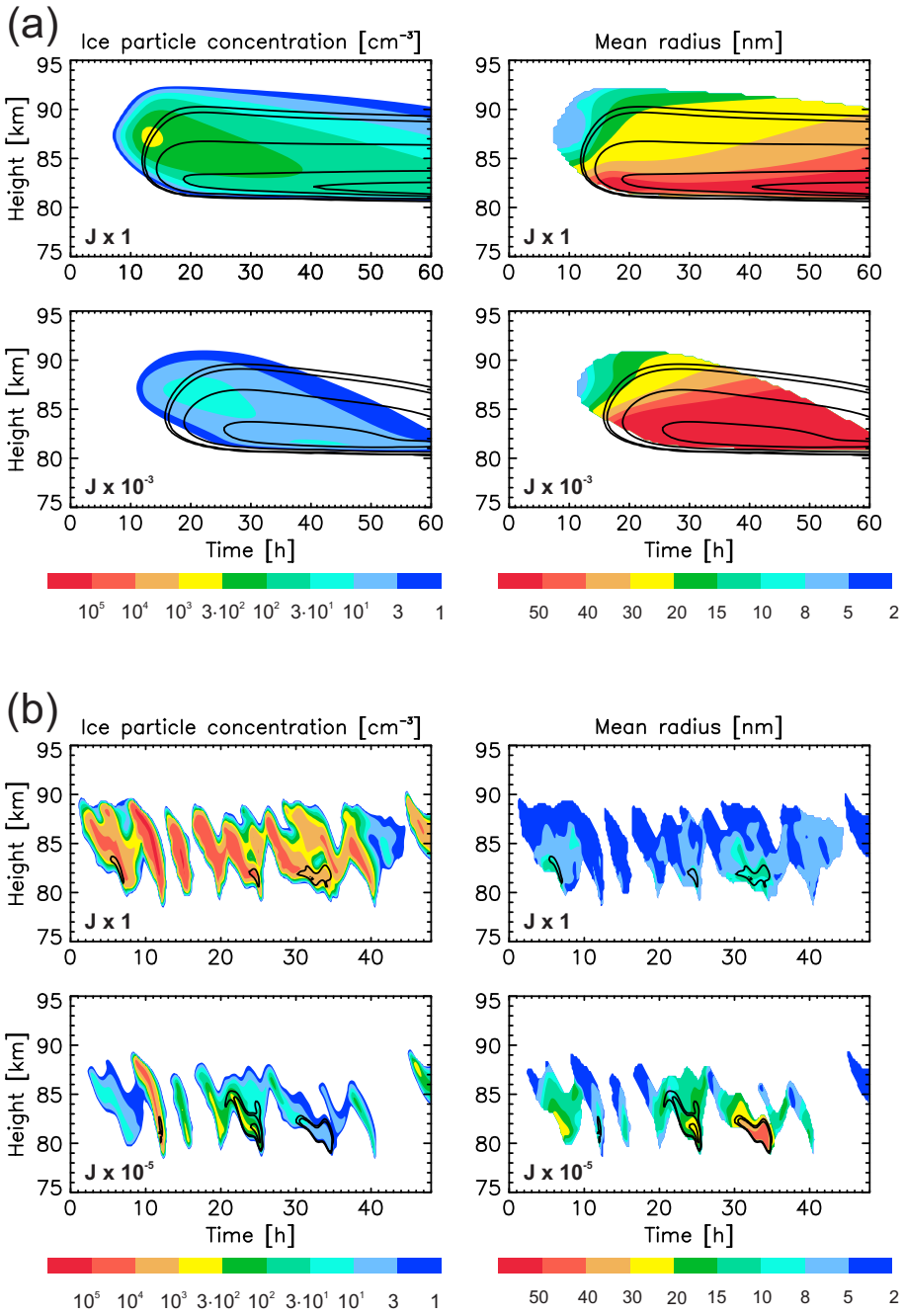

Figure 5. Sample CARMA simulation with (a) climatological and (b) wave driven background fields. The corresponding temperature and wind fields for the wave driven simulations are shown in Fig. 2 (b). The upper row in (a) and (b) is generated with the reference nucleation rate ($J \times 1$), the lower row with reduced nucleation rate ($J \times 10^{-3}$ and $J \times 10^{-5}$). The black contour lines indicate backscatter coefficients of (0.05, 0.1, 1, 10, 30) $\cdot 10^{-10}$ $\mathrm{sr}^{-1}\mathrm{m}^{-1}$.

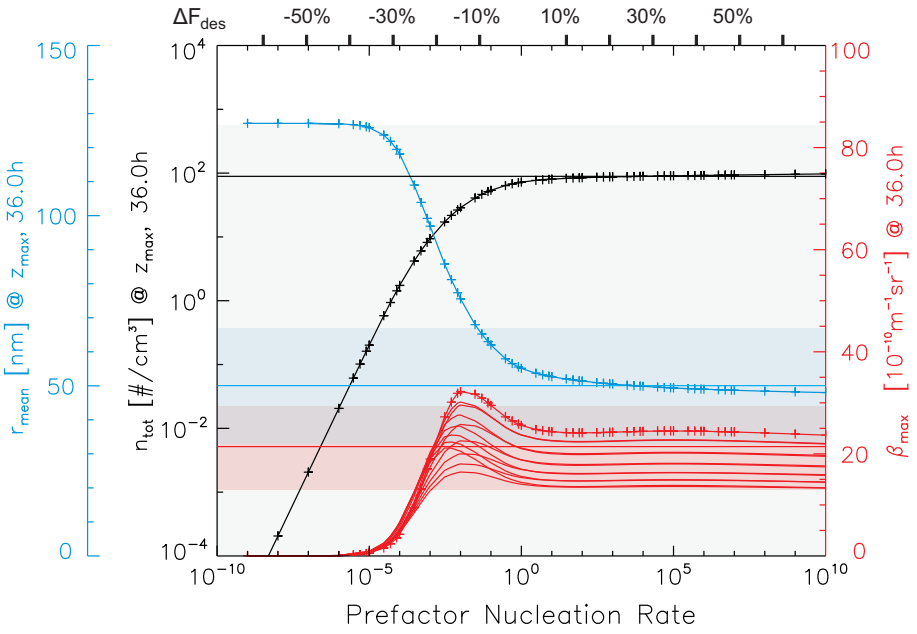

Figure 6. NLC properties in climatological background fields after 36 h of simulation time (24 h after the final temperature profile is reached) for different nucleation rate prefactors. Mean radius (blue) and total ice number density (black) are given at the altitude of the maximum backscatter coefficient. The backscatter coefficient (red) is shown for spheroidal ice particles with axis ratios between 1/7 and 7, spheres are indicated with crosses. The horizontal lines mark mean values for strong NLC and the shaded range their standard deviation derived by lidar measurements [*Baumgarten et al.*, 2008]. The upper scale indicates the change in percent of the desorption energy ΔF_{des} that leads to the according nucleation rate prefactor.

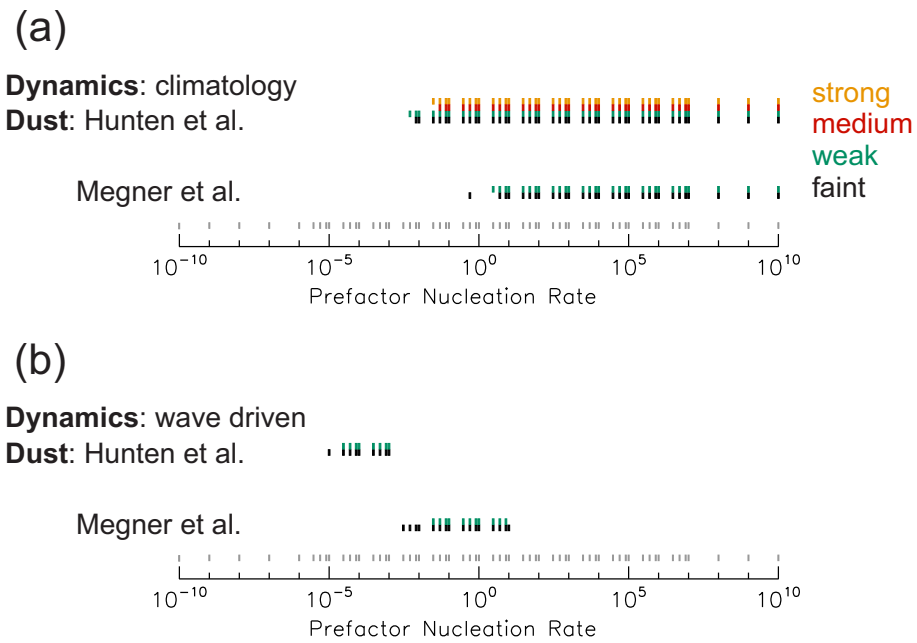

Figure 7. Overview over nucleation rate prefactors that lead to NLC comparable to lidar observations (see text for details). Simulations with (a) climatological background profiles for temperature and vertical wind are analyzed as well as simulations with (b) wave driven background fields of the KMCM. The simulations are initialized with either the MSP profile of *Hunten et al.* [1980] or *Megner et al.* [2008b] (top and bottom row in each panel). Gray marks above the abscissa indicate the prefactors implemented for this study.

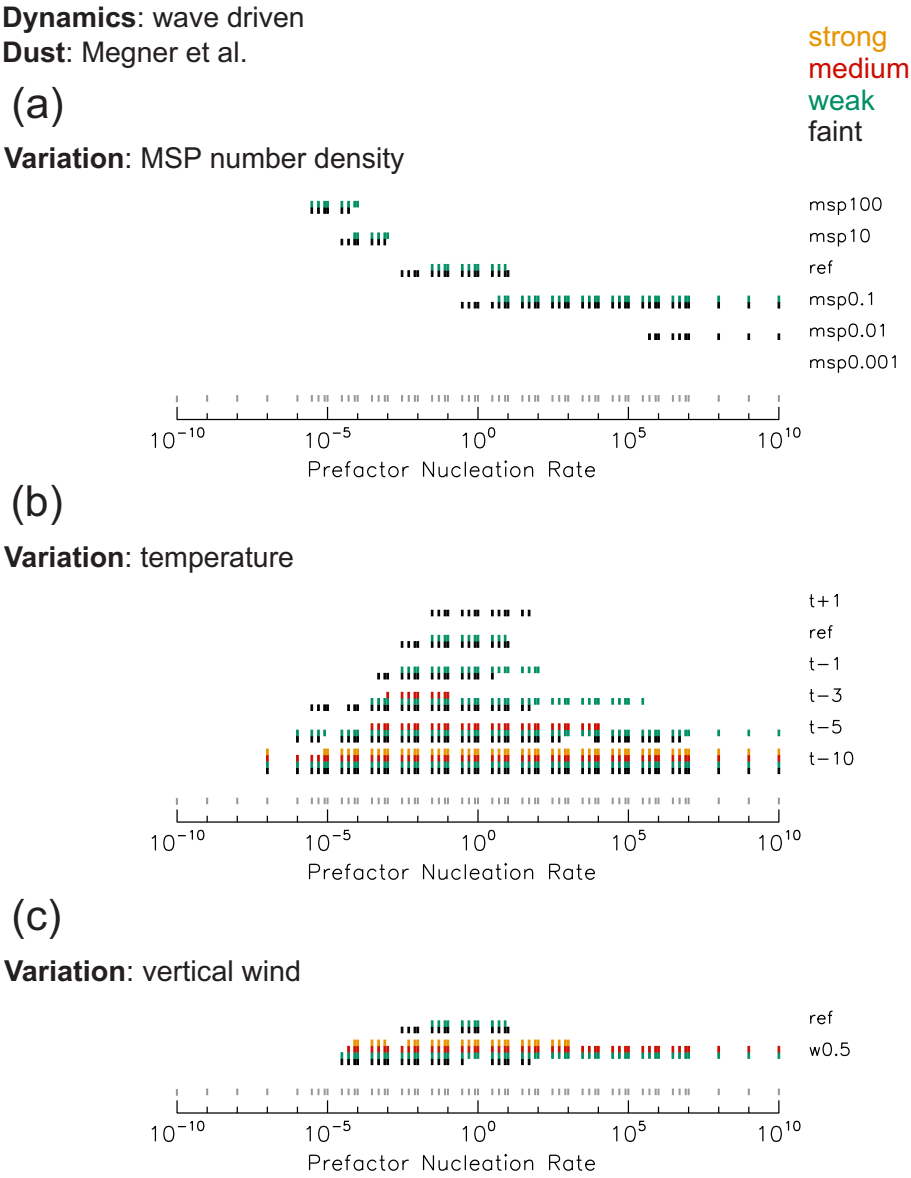

Figure 8. Overview over nucleation rate prefactors as in Figure 7 for changed background fields: (a) multiplication of the MSP profile with the factors 100, 10, 0.1, 0.01, and 0.001, (b) temperature profile shifted by −10 K, −5 K, −3 K, −1 K, and 1 K, (c) scaling of the vertical wind velocity by the factor of 0.5. The reference case (KMCM background fields and MSP profile of *Megner et al.* [2008b]) is labeled with 'ref'.

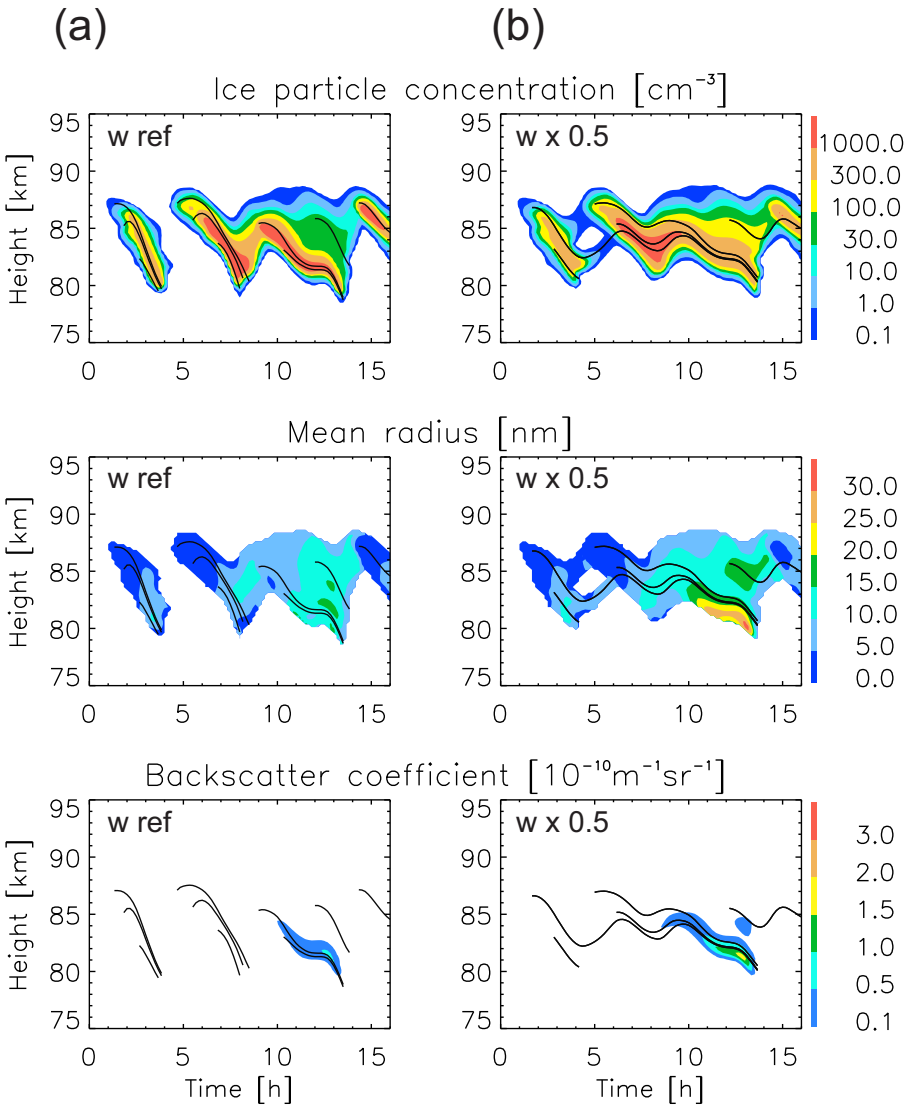

Figure 9. Visualization of tracer trajectories in (a) the reference wind field and (b) the wind field scaled by 0.5. NLC number density is shown in the top row, mean radius in the middle and backscatter coefficient in the lower row.

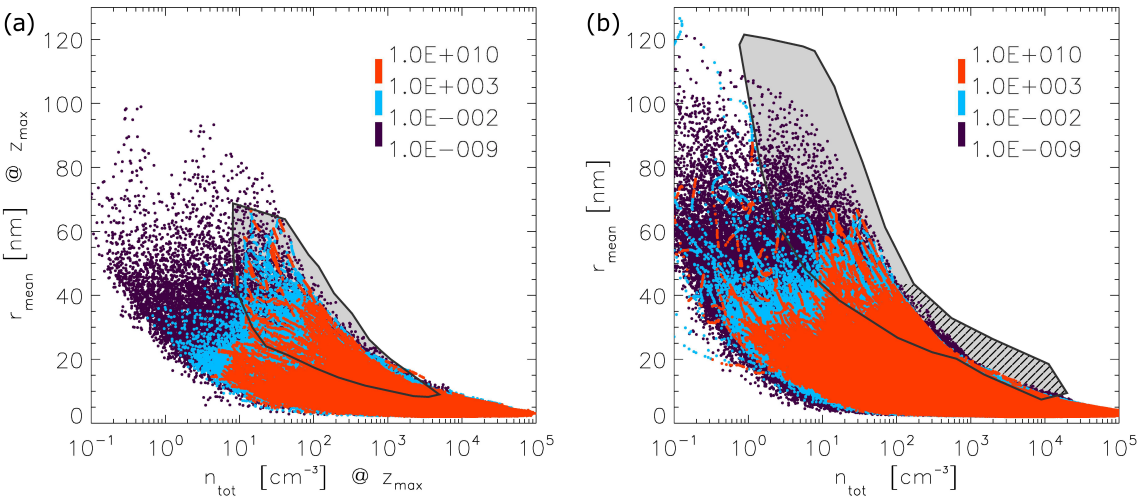

Figure 10. Distribution of modelled NLC in the $n_{\mathrm{tot}} - r_{\mathrm{mean}}$ plane at (a) the altitude of the maximum backscatter signal and (b) for all altitudes. The colors refer to different ranges of nucleation rate prefactors. Contour lines delimit the area where satellites have detected NLC: (a) *Hervig et al.* [2009a] and (b) *Hultgren and Gumbel* [2014]. In the hatched area comparatively few NLC were detected.

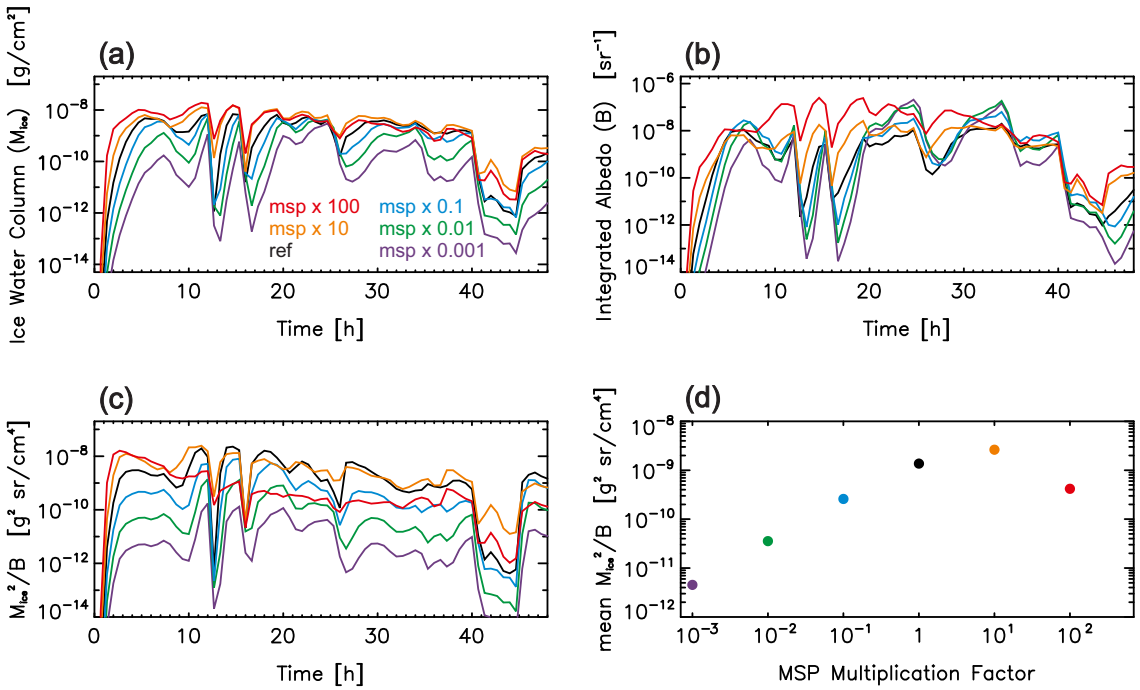

Figure 11. Temporal development of (a) ice water column M_{ice}, (b) integrated albedo B and (c) M_{ice}^2/B from the simulation shown in Fig. 5 (b) with prefactor 1. The number density of initial MSP is increased relative to the reference run by a factor of 10 and 100 and decreased by a factor of 0.1, 0.01 and 0.001. Time averaged values for M_{ice}^2/B are shown in panel (d) for the different MSP number densities.